Disrupted Mechanobiology Links the Molecular and Cellular Phenotypes in Familial Dilated Cardiomyopathy

Sarah R. Clippinger[1,2], Paige E. Cloonan[1,2], Lina Greenberg[1], Melanie Ernst[1], W. Tom Stump[1], Michael J. Greenberg[1,*]

[1] Department of Biochemistry and Molecular Biophysics, Washington University School of Medicine, St. Louis, MO, 63110, USA

[2] These authors contributed equally to this work

[*]Corresponding author:
Michael J. Greenberg
Department of Biochemistry and Molecular Biophysics
Washington University School of Medicine
660 S. Euclid Ave., Campus Box 8231
St. Louis, MO 63110
Phone: (314) 362-8670
Email: greenberg@wustl.edu

Running title: A DCM mutation disrupts mechanosensing

Keywords: Mechanosensing, stem cell derived cardiomyocytes, muscle regulation, troponin, myosin, traction force microscopy

27 **Abstract**

28 Familial dilated cardiomyopathy (DCM) is a leading cause of sudden cardiac death and a

29 major indicator for heart transplant. The disease is frequently caused by mutations of

30 sarcomeric proteins; however, it is not well understood how these molecular mutations

31 lead to alterations in cellular organization and contractility. To address this critical gap in

32 our knowledge, we studied the molecular and cellular consequences of a DCM mutation

33 in troponin-T, ΔK210. We determined the molecular mechanism of ΔK210 and used

34 computational modeling to predict that the mutation should reduce the force per

35 sarcomere. In mutant cardiomyocytes, we found that ΔK210 not only reduces contractility,

36 but also causes cellular hypertrophy and impairs cardiomyocytes' ability to adapt to

37 changes in substrate stiffness (e.g., heart tissue fibrosis that occurs with aging and

38 disease). These results link the molecular and cellular phenotypes and implicate

39 alterations in mechanosensing as an important factor in the development of DCM.

2

Introduction

DCM is a major cause of sudden cardiac death in young people, and it is a significant cause of heart failure (1). DCM is phenotypically characterized by dilation of the left ventricular chamber, and it is often accompanied by changes in cellular and tissue organization, including lengthening of individual myocytes and fibrosis-induced stiffening of the myocardial tissue. Genetic studies have demonstrated that familial DCM can be caused by single point mutations, many of which are in sarcomeric proteins responsible for regulating cardiac contractility (1); however, the connection between the initial insult of molecular-based changes in contractile proteins and the development of the cellular disease phenotype is not thoroughly understood. This lack of understanding has hampered efforts to develop novel therapeutics, and there is currently no cure for DCM, with heart transplantation being the only long-term treatment. The goal of this study was to better understand the connection between mutation-induced changes in contractility and the cellular phenotype.

Understanding the link between point mutations in sarcomeric proteins and the development of the disease phenotype in cells has been challenging for several reasons. One challenge stems from the fact that the clinical presentation and prognosis appear to depend on the specific mutation. In fact, different point mutations within the same molecule, and even different substitutions at the same amino acid site can lead to different forms of cardiomyopathy (e.g., hypertrophic, dilated, restrictive) with different ages of onset (2-5). Another challenge stems from selecting appropriate model systems of the human disease for the specific question being posed. *In vitro* biochemical studies are excellent for deciphering the molecular consequences of the initial insult (4); however,

63   they are not clearly predictive of how the disease will manifest itself in cells (6). Studies

64   using transgenic mice have significantly advanced our understanding of the disease;

65   however, these mice do not always recapitulate the human disease phenotype due to

66   differences in cardiac physiology between humans and mice (7-13). Patient tissue is

67   excellent for studying the disease phenotype in humans (14); however, tissue from

68   patients is difficult to obtain and usually only available from patients in the end stages of

69   the disease or post mortem, when compensatory mechanisms can mask the initial insult.

70   Recent advances in stem cell (15, 16) and gene editing technologies (17) have

71   provided a new avenue for modeling DCM in human pluripotent stem cell derived

72   cardiomyocytes (hPSC-CMs) (18, 19). These hPSC-CMs can faithfully recapitulate many

73   aspects of the early human disease (20), making them an excellent tool for deciphering

74   how the initial molecular insult leads to the development of the early disease phenotype.

75   Moreover, these cells can be examined in simplified *in vitro* systems that mimic various

76   aspects of the environment in the heart to dissect how the local environment influences

77   the development of the disease phenotype. It has been shown that cardiomyocytes can

78   adapt their contractility in response to their local mechanical and geometric environment

79   (21-23). It is possible aberrant responses of cardiomyocytes to disease-related alterations

80   in the local environment such as fibrosis-induced stiffening of the heart tissue could

81   contribute the development of the disease phenotype.

82   To uncover the connection between molecular changes and the development of

83   the cellular disease phenotype, we determined the molecular and cellular mechanisms of

84   a DCM-causing point mutation in the protein troponin-T (TNNT2), deletion of lysine 210

85   (ΔK210) (24) (Figure 1A). The ΔK210 mutation has been identified in patients as young

86   as 2 years old in at least four unrelated families (25-27). Troponin-T is a subunit of the

87   troponin complex, which, together with tropomyosin, regulates the calcium-dependent

88   interactions between the force-generating molecular motor myosin and the thin filament.

89   TNNT2 is one of the most frequently mutated genes in DCM (28, 29). There have been

90   several excellent model systems developed to better understand aspects of the disease

91   caused by this mutation (30-34). However, the connection between the molecular

92   mutation and the cellular phenotype seen in humans remains unclear.

93   Our results demonstrate that ΔK210 causes a reduction in myosin-based force

94   generation at the molecular and cellular levels, and we used computational modeling to

95   link the contractile phenotypes seen at these scales. Surprisingly, we found that this

96   disease-causing mutation of a sarcomeric protein not only impairs cardiomyocyte

97   contraction, but it also causes cellular hypertrophy and impairs the ability of

98   cardiomyocytes to sense and respond to changes in their mechanical environment. Our

99   results suggest a central role for defects in mechanosensing in the disease pathogenesis.

100 **Results**

101 **ΔK210 decreases calcium sensitivity in an *in vitro* motility assay**

102 We set out to decipher the molecular mechanism of the ΔK210 mutation *in vitro*.

103 The molecular effects of cardiomyopathy mutations depend on the myosin isoform (7-9,

104 35-37) and therefore, we used porcine cardiac ventricular myosin (38). Porcine ventricular

105 cardiac myosin (MYH7) is 97% identical to human, while murine cardiac myosin (MYH6)

106 is only 92% identical. Porcine cardiac myosin has very similar biophysical properties to

107 human cardiac myosin, including the kinetics of the ATPase cycle, step size, and

108 sensitivity to load (38-41), making it an ideal myosin for biophysical studies.

109 Given the role of troponin-T in thin filament regulation, we first determined whether

110 the ΔK210 mutation affects calcium-based regulation of myosin binding to thin filaments

111 using an *in vitro* motility assay (42). Reconstituted thin filaments, consisting of porcine

112 cardiac actin and recombinantly expressed human troponin and tropomyosin, were added

113 to a flow cell coated with porcine cardiac myosin in the presence of ATP. The speed of

114 filament translocation was measured as a function of added calcium. As has been

115 reported previously, the speed of regulated thin filament translocation increased

116 sigmoidally with increasing Ca^{2+} concentration (43), (Figure 1B). Data were fit with the Hill

117 equation to obtain the pCa50 (i.e., the concentration of calcium necessary for half-

118 maximal activation). Consistent with previous studies using mouse cardiac, rabbit cardiac,

119 and rabbit skeletal muscle fibers (31, 33, 44), ΔK210 shows a right-shifted curve (pCa50

120 = 5.7 ± 0.1) compared to the WT (pCa50 = 6.1 ± 0.1; $p < 0.0001$), meaning more calcium

121 is needed for the same level of activation. This suggests that the mutant could show

122 impaired force production during a calcium transient.

6

123

Molecular mechanism of ∆K210-induced changes in thin filament regulation

125   The changes in calcium sensitivity seen in the *in* vitro motility assay could be due

126   to alterations in thin-filament based regulation or allosteric effects on myosin's kinetics.

127   To test whether the mutation affects the kinetics of myosin dissociation from thin

128   filaments, we measured the rate of ADP release from myosin, the transition that limits

129   actomyosin dissociation at saturating ATP in the absence of load (45). Consistent with

130   previous studies of other DCM troponin mutations (46), ∆K210 does not change the

131   kinetics of ADP release from myosin, (Figure 1 – figure supplement 1), and therefore, the

132   primary effects of the mutation are likely due to alterations in thin filament-based

133   regulation.

134   Biochemical (47) and structural biological (48, 49) experiments have shown that

135   thin filament regulation is a complicated process where tropomyosin can lie along the thin

136   filament in three positions (blocked, closed, and open), and that this positioning is

137   determined by both calcium and myosin binding (Figure 2A). To determine the molecular

138   mechanism of the observed changes in the calcium sensitivity of myosin-based motility,

139   we determined the equilibrium constants for the transitions between these states.

140   The equilibrium constant for the transition between the blocked and closed states,

141   K_B, was measured using stopped-flow kinetic techniques (47), where the rate of myosin

142   binding to pyrene-labeled regulated thin filaments was measured at high (pCa 4) and low

143   (pCa 9) calcium concentrations. Myosin strong binding to labeled thin filaments quenches

144   the pyrene fluorescence, leading to a roughly exponential decrease in fluorescence

7

145 (Figure 2B-C). The ratio of the rate constants for myosin binding to the thin filament at

146 high and low calcium can be used to calculate the equilibrium constant, K_B (47):

147
$$\frac{k_{obs}(-Ca^{2+})}{k_{obs}(+Ca^{2+})} \approx \frac{K_B}{1 + K_B} \quad (Eq.\,1)$$

148 The values of K_B obtained were 0.36 ± 0.15 for WT (n=3) and 0.36 ± 0.10 for ∆K210 (n=3),

149 indicating that ∆K210 does not significantly affect the equilibrium constant for the

150 transition between the blocked and closed states (p = 0.99).

151   To determine the equilibrium constant for the transition between the closed and

152 open states, K_T, we measured the steady-state binding of myosin to pyrene-labeled

153 regulated thin filaments over a range of myosin concentrations (Figure 2D-E). Titration

154 relationships obtained for WT and ∆K210 at high (pCa 3) and low (2 mM EGTA) calcium

155 concentrations show two-state (i.e., no calcium-based blocking) and three-state

156 processes, respectively, as has been observed previously (47). Five technical replicates

157 were used to define each curve. As described in the Materials and Methods, we modified

158 the fitting and analysis procedure used by McKillop and Geeves to better define the values

159 of the fitted variables (50). We performed an additional titration at an intermediate calcium

160 concentration (pCa 6.25) and used an annealing algorithm to globally fit the binding

161 curves of the fractional change in pyrene fluorescence (a) as a function of myosin

162 concentration for all three calcium concentrations (Figure 2D-E). The fractional change in

163 the pyrene fluorescence is given by (47):

164
$$a = \frac{F_0 - F}{F_0 - F_\infty} = \frac{K_W[M]P^{n-1}(K_T(1 + K_S)^n + 1)}{(K_T P^n + Q^n + \frac{1}{K_B})(1 + K_S)^{n-1}} \quad (Eq.\,2)$$

165 where [M] is the concentration of myosin, F is the measured fluorescence, F_0 is the

166 fluorescence in the absence of myosin, F_∞ is the fluorescence at saturating myosin

8

167   concentrations, n is the size of the cooperative unit, $P=1+K_W[M](1+K_S)$, and $Q=1+K_W[M]$

168   (Figure 2D-E). For the fitting, K_T, K_W (i.e., the equilibrium constant between the open and

169   myosin weakly bound states, sometimes denoted K_1), and n were fit parameters. K_B and

170   K_S (the equilibrium constant between the myosin weakly and strongly bound states,

171   sometimes denoted K_2) were fixed based on the calculated values for K_B (Figure 2B-C)

172   and previously measured values of K_S (51). 95% confidence intervals were calculated

173   from 1000 rounds of bootstrapping simulations (see Materials and Methods).

174   We found that while the measured values of K_T for ∆K210 were consistently lower

175   compared to the WT at all calcium concentrations (Figure 3A), only the difference in K_T

176   at pCa 6.25 was statistically significant (p=0.028). From the measured equilibrium

177   constants, it is straightforward to calculate the fraction of regulatory units in each state

178   from the partition function. At all calcium concentrations, ∆K210 shows a decrease in the

179   fraction of thin filaments in the open, weakly-bound, and strongly-bound states compared

180   to the WT (Figure 3B), and an increase in the fraction of thin filaments in the blocked and

181   closed states. These data give the biochemical mechanism of the reduced activation at

182   sub-saturating calcium seen in the *in vitro* motility assays (Figure 1B).

183

184   **Computational modeling recapitulates the shift in calcium sensitivity and predicts**

185   **a lower force per sarcomere for ∆K210**

186   To connect how the observed changes in the equilibrium populations of thin

187   filament regulatory units with contractility in a sarcomere, we used a computational model

188   developed by Campbell et al. (52). Given a set of equilibrium constants for thin filament

189   activation, this model calculates both the steady-state force as a function of calcium and

9

190   the force produced per sarcomere in response to a calcium transient. Using our measured

191   equilibrium constants, the steady-state normalized force was simulated for both WT and

192   ΔK210 over a range of calcium concentrations (Figure 4A). Simulation of ΔK210 shows a

193   rightward shift towards supermaximal calcium activation, consistent with the shift seen in

194   the *in vitro* motility assay (Figure 1B). Therefore, the observed set of changes in the

195   equilibrium constants in the mutant can mechanistically explain the observed changes

196   seen in the *in vitro* motility assay, validating the approach taken here.

197   To predict the effects of the ΔK210 mutation on the force per sarcomere, we used

198   the same computational model to simulate the force per sarcomere in response to a

199   calcium transient. In the modeling, we assumed that the primary effects of the mutation

200   are on thin filament positioning, and that to a first order approximation, the calcium

201   transient is not significantly changed by the mutation. The consequences of these

202   assumptions are explored in the Discussion. The simulation shows a smaller maximal

203   twitch force per sarcomere in response to a calcium transient for ΔK210 compared to the

204   WT (Figure 4B). Taken together, these simulations predict that ΔK210 should decrease

205   the force per sarcomere in cardiomyocytes.

206

207   **Generation of ΔK210 induced stem cell-derived cardiomyocytes**

208   To examine the effects of the ΔK210 mutation in human cells, we generated human

209   induced pluripotent stem cell (hPSC)-derived cardiomyocytes (hPSC-CMs). The hPSC

210   lines were derived from the BJ foreskin fibroblast line by the Washington University

211   Genome Engineering core (see Materials and Methods). Whole exome sequencing of the

212   stem cell line demonstrated that these cells do not have any genetic variants associated

10

213   with familial cardiomyopathies (Figure 5 – figure supplement 1). Cell lines homozygous

214   for the ΔK210 mutation were generated using the CRISPR/Cas9 system (17) (Figure 5 –

215   figure supplement 2) (see Materials and Methods). ΔK210 mutant stem cells have normal

216   karyotypes (Figure 5 – figure supplement 3) and are pluripotent, as assessed by

217   immunofluorescence staining for pluripotency markers (Figure 5 – figure supplement 4).

218   For all experiments with the mutant hPSC-CMs, two separate stem cell lines were used

219   to ensure that the observations are not due to potential off-target cuts introduced during

220   the CRISPR/Cas9 editing. We also used hPSC-CMs from at least two separate

221   differentiations per cell line for both WT and ΔK210. hPSCs were differentiated to hPSC-

222   CMs using established protocols (15, 53) involving temporal modulation of WNT signaling

223   using small molecules (Figure 5 -figure supplement 5) and aged at least 30 days before

224   use. Using this procedure, >90% cardiomyocytes were obtained, as determined by

225   immunofluorescence staining for cardiac troponin-T (Figure 5 -figure supplement 5).

226   To examine the sarcomeric organization of hPSC-CMs, cells cultured on glass

227   were fixed and stained for troponin-I and α-actinin to visualize the thin filament and z-

228   discs, respectively (Figure 5). Unlike adult human tissue derived cardiomyocytes, which

229   are rectangular with sarcomeres that align with the long axis of the cell, WT hPSC-CMs

230   cultured on glass orient randomly and display robust sarcomeric staining that is typically

231   not aligned along a single axis (Figure 5A). Compared to the WT hPSC-CMs, ΔK210

232   hPSC-CMs display more disorganized sarcomeres with patches of punctate staining

233   (Figure 5B). Similar disorganization and punctate sarcomere structure has been seen

234   with other hPSC-CM models of DCM cultured on stiff substrates (6, 18, 54), suggesting

235   that it might be a common feature of some forms of DCM.

236

237 **ΔK210 hPSC-CMs show a pronounced increase in size and mechanosensitive**

238 **alterations in sarcomeric structure**

239 Cardiomyocytes are sensitive to their local physical environment, and it has been

240 shown that providing physical cues that mimic the environment of the heart can improve

241 cardiomyocyte structure and contractility (21, 55). During aging and DCM disease

242 progression, the heart becomes stiffer, and the myocytes become disordered. We

243 hypothesized that ΔK210 hPSC-CMs would show aberrant responses to changes in their

244 physical environment. To test this hypothesis, we examined the size and structure of cells

245 on glass, which has a high stiffness (~GPa) and on hydrogel substrates with a stiffness

246 matched to healthy heart tissue (10 kPa).

247 To examine the role of geometric cues in cellular organization, we micropatterned

248 extracellular matrix for cellular adhesion in rectangular patterns with a 7:1 aspect ratio

249 (21). We examined live cells using bright field microscopy, and fixed cells stained for the

250 z-disc marker α-actinin and troponin-I using confocal microscopy (Figure 5C-F).

251 Interestingly, the ΔK210 hPSC-CMs are significantly larger than the WT in fixed cells on

252 glass (Figures 5 and 6), fixed cells on 10 kPa hydrogels (Figures 5 and 6), and in live

253 cells on 10 kPa hydrogels (Figures 5 and 7). We analyzed a large number of cells and

254 generated cumulative distributions of cell sizes for single cells, since this methodology

255 does not assume a form for the underlying distribution (Figures 6 and 7). The cumulative

256 distribution shows the fraction of cells with an area less than or equal to the value of the

257 x-axis. The increase in size is due to increases in both cell width and length (Table 1,

12

258 Figure 6). These data demonstrate that ΔK210 hPSC-CMs are larger than the WT cells,

259 and that this increase in size is not dependent on the mechanical environment.

260 Next, we examined the influence of substrate stiffness on the sarcomeric

261 organization of ΔK210 hPSC-CMs. We fixed and stained micropatterned hPSC-CMs for

262 the sarcomeric marker α-actinin on both glass and 10 kPa substrates. Both WT and

263 ΔK210 hPSC-CMs sarcomeres orient preferentially along the long axis of the cells

264 patterned on glass and on 10 kPa hydrogels (Figure 5). To quantify the degree of

265 sarcomeric organization, we used a program developed by Pasquilini et al. (55). The

266 program analyzes fluorescence images with periodic structure, and it calculates the

267 orientational order parameter, OOP (i.e., the fraction of z-discs that are oriented along a

268 single axis). For cells with z-discs all oriented along a single axis, OOP=1, and for cells

269 with z-discs with no preferred axis, OOP=0.

270 When patterned on glass (GPa stiffness), the ΔK210 mutant hPSC-CMs show a

271 reduction in the fraction of sarcomeres aligned along the long axis compared to the WT

272 ($p = 0.008$) (Figure 6A, Table 1). This is consistent with what we saw with unpatterned

273 cells on glass (Figure 5A-B). Strikingly, when patterned on hydrogels that mimic the

274 stiffness of healthy heart tissue, the ΔK210 cells show significantly improved sarcomeric

275 organization (Figure 6B, Table 1). As quantified using the OOP, the organization of the

276 ΔK210 sarcomeres are indistinguishable from the WT on 10 kPa substrates ($p = 0.5$).

277 Taken together, these results demonstrate that the ΔK210 mutation affects how the

278 hPSC-CMs respond to their mechanical environment, with ΔK210 cells showing normal

279 sarcomeric organization on physiological stiffness substrates, but reduced sarcomeric

280 organization on stiff substrates.

13

281

282   **∆K210 cells show altered contractility and features of hypertrophy on substrates**

283   **of physiological stiffness**

284   Our computational modeling predicts that ∆K210 cells should show a lower force

285   per sarcomere (Figure 4B); and therefore, we examined whether the ∆K210 mutation

286   affects force production of single hPSC-CMs. To measure force production of single

287   hPSC-CMs, we used traction force microscopy. Spontaneously beating cells were

288   micropatterned onto 10 kPa hydrogels prepared with embedded fluorescent microbeads

289   to monitor beating. Spinning disk confocal imaging was used to monitor the bead

290   displacement as a function of time, and the total force of contraction for each cell was

291   calculated using a MATLAB routine developed by Ribeiro et al. (56) (Figure 7B-C). For

292   each cell, the force per sarcomere was approximated by calculating the force per area.

293   The average total force per cell measured by traction force microscopy was the

294   same for both WT (0.27 (-0.03/+0.04) μN) and ∆K210 hPSC-CMs (0.27 (-0.04/+0.05) μN;

295   p = 0.98) (Figure 7C). For each cell analyzed by traction force microscopy, we measured

296   its area from bright-field illumination images (Figure 7A). Bright-field images of live cells

297   lack the resolution of the immunofluorescence images, making it impossible to accurately

298   measure the cross-sectional area of the live cells; however, ∆K210 hPSC-CMs are

299   significantly larger than the WT cells (Figure 7A). Moreover, fixed ∆K210 hPSC-CMs on

300   10 kPa hydrogels have a sarcomeric organization that is indistinguishable from the WT

301   (Figure 6B). We calculated the force per area for each cell (Figure 7B). The ∆K210 cells

302   have a lower force per area (0.25 (-0.04/+0.05) μN/μm^2) compared to the WT (0.32 (-

303   0.04/+0.04) μN/μm^2; p = 0.01). The lower force per area for ∆K210 is consistent with our

14

304   molecular studies and the computational prediction of a lower force per sarcomere (Figure

305   4B). These data link our molecular and cellular phenotypes. Moreover, they demonstrate

306   that although the force per sarcomere is reduced in the mutant, the ΔK210 hPSC-CMs

307   can compensate through an increase in size that results in a total force per cell that is

308   indistinguishable from the WT.

309
310

311   **Discussion**

312   Here, we determined the mechanism of a mutation in troponin-T that causes DCM

313   in humans, ΔK210. We found that this mutation affects not only molecular and cellular

314   contractility, but also the ability of the cardiomyocytes to respond to changes in the

315   mechanical environment like stiffening of heart tissue associated with aging and disease

316   in patients. These results implicate defective mechanosensing as an important factor in

317   the pathogenesis of DCM caused by mutations in sarcomeric proteins, and they highlight

318   the importance of multiscale studies in understanding heart disease.

319

320   **Proposed molecular mechanism for ΔK210 and its relationship to previous studies**

321   The disease presentation of familial cardiomyopathies and their biophysical

322   manifestation (i.e., contractile and force-dependent properties) can depend on the myosin

323   isoform (7, 8, 57-60). Our *in vitro* motility results (Figure 1B) using porcine cardiac actin

324   and ventricular β-cardiac muscle myosin (MYH7), which closely mimics the biophysical

325   and biochemical properties of human ventricular β-cardiac muscle myosin (38, 39),

326   demonstrate a shift towards supermaximal calcium activation, consistent with previous

327   experiments studying the ΔK210 using different myosin isoforms (31, 44).

328   We determined that this shift is due to alterations in the equilibrium constants that

329   govern the positioning of tropomyosin along the thin filament, leading to a reduction in the

330   population of force-generating cross bridges at submaximal calcium concentrations

331   (Figures 3 and 4A). The structural basis of these mutation-induced shifts is not well

332   understood; however, it is possible that the mutation affects the interaction between the

333   troponin complex and tropomyosin (61) and/or the allosteric coupling between subunits

334   of the troponin complex (2, 5, 62, 63). These non-exclusive mechanisms could contribute

335   to the observed decrease in force-producing states seen in ΔK210 thin filaments, and

336   future studies should be able to shed light on the structural basis of these changes.

337   Our data were analyzed using the formalism developed by McKillop and Geeves

338   (47). Other models of thin filament regulation exist (64-68), but the McKillop and Geeves

339   model is one of the most frequently used. Due to the nature of our experimentation, it is

340   not possible to directly compare our results with those from other models of thin filament

341   regulation. However, the computational simulations based on the McKillop and Geeves

342   model are able to recapitulate the shift in calcium sensitivity seen in the motility assay

343   (Figures 1B and 4A).

344   The computational modeling based on our biochemical studies predicts a larger

345   reduction in the force per sarcomere than we observed in cells (Figure 7). This is likely

346   due to several necessary simplifying assumptions made in the modeling: 1) We assumed

347   that the mutation does not change the magnitude or time course of the calcium transient,

348   which is not necessarily true given that the knock-in ΔK210 mouse shows altered calcium

349   transients (31). 2) We assumed that the troponin in hPSC-CMs has the same biochemical

350   properties as the adult cardiac troponin complex that we examined in our biochemical

351   experiments. This is not necessarily the case, since four troponin-T isoforms can be

352   detected in the human heart at different developmental stages (69, 70), and hPSC-CMs

353   primarily express a slow skeletal muscle isoform of troponin-I (71), rather than the cardiac

354   isoform used in the biochemical studies. While all isoforms of troponin expressed in

355   hPSC-CMs would have the ΔK210 mutation (Figure 5 – figure supplement 2), different

356   isoforms have different calcium sensitivities (69). That said, even with these simplifying

357   assumptions, the simulations were able to predict the reduction in the force per sarcomere

358   seen in the ΔK210 cardiomyocytes.

359

360   **Linking the molecular and cellular contractile phenotypes for ΔK210**

361   Patients with the ΔK210 mutation show early onset of the disease phenotype and

362   a high incidence of sudden death (26). Aspects of the disease have been replicated in

363   knock-in mouse models (31), which have significantly advanced our understanding of the

364   disease phenotype. However, the ΔK210 mouse model shows significant differences with

365   respect to the human phenotype, due to inherent physiological differences between

366   mouse and human hearts, including differences in gene expression, calcium-handling

367   machinery, and ion channel composition (34).

368   We used human hPSC-CMs to study how the initial insult of a molecular-based

369   change leads to the early disease pathogenesis in human cells. For these studies, hPSC-

370   CMs are excellent models, since they can capture cellular changes that occur before

371   major compensatory mechanisms (e.g., fibrosis, activation of neurohormonal pathways,

372   changes in gene expression) mask the initial molecular phenotype (18-20, 54, 72).

373   Contractile changes associated with the disease have been observed in cardiomyopathy

374   patients before adverse remodeling of the heart (73-75). That being said, hPSC-CMs are

375   developmentally immature, meaning that they do not necessarily recapitulate all the

376   aspects of the phenotype in adults or the later stages of the disease progression. All of

377   our molecular and cellular studies modeled the homozygous ΔK210 mutation, so care

378   should be used when extrapolating the results here to the phenotype seen in patients.

18

379   ∆K210 hPSC-CMs show a reduced force per area compared to WT cells (Figure

380   7B). We did not see any differences in the sarcomeric organization of mutant cells on

381   patterned hydrogels (Figure 6B), suggesting that the observed reduction in the force per

382   area is due to a reduction in the force per sarcomere. This result is consistent with the

383   results of our computational modeling of our biochemical measurements (Figure 4B), and

384   it links the molecular phenotype with cellular contractility.

385   Interestingly, while the force per sarcomere is reduced in the mutant, the total force

386   per cell is not different from the WT (Figure 7C). This can be explained by the fact that

387   the mutant cells are larger (Figures 6, 7), a result that would not have been predicted from

388   the molecular studies alone. This increase in size occurs in single cells, independent of

389   endocrine or cell-cell signaling. One possible explanation for this increase in size is that

390   the cells are undergoing compensatory hypertrophy, which allows the cells to counteract

391   the reduced force per sarcomere. While we have not investigated whether the increase

392   in size seen in our cells is due to activation of hypertrophic signaling, future studies should

393   elucidate the mechanism of the increase in cell size seen here.

394

395   **Defects in ∆K210 mechanosensing contribute to the disease phenotype**

396   Fundamentally, troponin serves as a gate that regulates myosin-based tension. As

397   such, one would expect that the primary effects of the mutation would be to reduce force

398   production; however, the ∆K210 cells show several changes beyond altered contractility.

399   While healthy cardiomyocytes adapt their contractility and structure to changes in their

400   mechanical environment, such as age or disease-related stiffening of the heart tissue

401   (21), ∆K210 cells do not adapt in the same way as the WT cells. Similar to other hPSC-

19

402 CM models of DCM grown on stiff substrates, ΔK210 hPSC-CMs cultured on glass show

403 impaired sarcomeric organization (18, 54, 76); however, ΔK210 hPSC-CMs can organize

404 normally when given mechanobiological cues that mimic the healthy heart (Figures 5 and

405 6). Therefore, the ΔK210 mutation affects not only contractility, but also the ability of the

406 hPSC-CMs to sense and respond to their environment.

407 The connection between the reduction in myosin-generated tension in the mutant

408 cells and an impaired ability to respond to mechanical forces warrants further

409 investigation; however, a possible link between cellular tension and sarcomeric

410 organization in DCM was revealed by live-cell imaging of sarcomerogenesis in hPSC-

411 CMs (54). It was shown that pharmacological inhibition of myosin contractility or genetic

412 disruption of titin leads to an impaired ability of cells to generate well-organized

413 sarcomeres. Chopra et al. proposed that the transduction of myosin-driven tension is

414 necessary for the proper assembly of sarcomeres. We propose that a similar mechanism

415 could be relevant in ΔK210 cells, which show reductions in myosin-based contractility and

416 sarcomeric disorganization when patterned on glass. Consistent with this idea, treatment

417 of hPSC-CMs containing a different DCM mutation with Omecamtiv mecarbil, a myosin-

418 based thin filament activator (41, 77, 78), leads to an improvement in sarcomeric

419 organization (76). We speculate that some of the salutary effects of the drug are due to

420 the restoration of tension necessary for proper mechanosensing.

421 The result that ΔK210 hPSC-CMs show altered responses to changes in their

422 mechanical environment has important implications for the mechanism of the disease

423 pathogenesis. Previous studies of cardiomyocytes have shown that the organization of

424 sarcomeres varies depending on substrate stiffness (21, 76), with peak contractility

425   occurring on substrates of physiological stiffness. ΔK210 hPSC-CMs can organize

426   properly and they have normal force production on substrates that match the stiffness of

427   the healthy heart (Figures 6 and 7); however, heart tissue becomes stiffer with the disease

428   progression and aging. We propose that as the heart tissue becomes stiffer, ΔK210 cells

429   would become more disordered, effectively causing a progressive loss of function, and

430   potentially contributing to myocyte disarray. Thus, the inability of the mutant cells to adapt

431   to changes in their mechanical environment may contribute to the disease pathogenesis

432   and progression.

433

434   **The potential importance of mechanosensing in DCM pathogenesis**

435   Our results suggest that reduced force at the molecular scale can lead to impaired

436   mechanosensing in cardiomyocytes. While the disease presentation in DCM depends on

437   the exact mutation (79), we propose that disruption of mechanosensing could be a

438   common mechanism in the disease pathogenesis of other sarcomeric and non-

439   sarcomeric DCM mutations. It has been proposed that DCM can be caused by molecular

440   hypocontractility (4, 80, 81); however, there are also many DCM-causing mutations in

441   non-sarcomeric genes with no known roles in contractility; suggesting that other

442   mechanisms might be involved (1, 3, 82). Most, but not all, of these genes are located

443   along proposed mechanosensing pathways (83, 84) used to sense and transduce

444   mechanical forces. For example, some of these genes link the cytoskeleton to the

445   extracellular matrix (e.g., dystrophin (DMD), vinculin (VCL)), others link the cytoskeleton

446   to the nucleus (e.g., nesprin-1 (SYNE1), lamin-A (LMNA), centromere protein F (CENP-

447   F)), and others are mechanosensitive transcription factors (e.g., TAZ). Consistent with

21

448   this idea, altered mechanobiology has been identified in DCM cells with mutations in the

449   non-sarcomeric protein lamin (82). Moreover, patients with mutations in these genes,

450   such as those with Duchenne muscular dystrophy and Emery-Dreifuss muscular

451   dystrophy, often develop DCM. It is intriguing to speculate that impaired mechanosensing

452   by cardiomyocytes in the heart could link some of these seemingly different diseases.

453

454   **Conclusions**

455   Using a combination of biochemical, computational, and cell biological techniques,

456   we reveal several features of a DCM mutation that would have been missed by studying

457   the molecular or cellular phenotypes alone. We demonstrate that the ΔK210 mutation in

458   human cardiac troponin-T causes a change in the equilibrium positioning of tropomyosin,

459   leading to alterations in the calcium sensitivity of thin filament activation. Computational

460   modeling predicted that these changes should lead to a reduction in the force generated

461   per sarcomere in mutant cells, and we demonstrate that this is indeed the case in hPSC-

462   CMs. Moreover, our results demonstrate that the ΔK210 mutation affects the structural

463   organization of hPSC-CMs and alters how they respond to their mechanical environment.

464   Finally, we demonstrate that the ΔK210 hPSC-CMs can increase in size to normalize their

465   force production. Taken together, these results demonstrate that disease-causing

466   mutations of sarcomeric proteins affect not only contraction, but also how cardiomyocytes

467   sense and respond to changes in their mechanical environment associated with aging

468   and disease. These data also suggest that disrupting mechanosensing pathways can

469   contribute to the disease phenotype in DCM.

470

482

Competing interests:

484 All experiments were conducted in the absence of any commercial or financial

485 relationships that could be construed as a potential conflict of interest.

486

Author contributions:

488 S.R.C. purified proteins, performed and analyzed the stopped flow and fluorescence

489 experiments, and drafted the manuscript. P.E.C. performed and analyzed the

490 fluorescence and traction force microscopy experiments with the stem cell derived

491 cardiomyocytes. L.G. purified proteins, performed *in vitro* motility assays, implemented

492 the cell-based assays, and performed and analyzed experiments with stem cell derived

493 cardiomyocytes. M.E. performed and analyzed fluorescence microscopy experiments.

23

494   W.T.S. designed tools for microcontact printing. M.J.G. oversaw the project, generated

495   mutant proteins, implemented biochemical assays, analyzed data, and drafted the

496   manuscript. All authors contributed to the editing of the final manuscript.

497

498 **Materials and Methods**

499 <u>Tissue purification of proteins for *in vitro* biochemical experiments</u>

500 Porcine cardiac myosin and actin were simultaneously purified from cryoground porcine

501 ventricles (Pelfreez) as previously described (38). Myosin subfragment-1 (S1) was

502 prepared by chymotrypsic digestion of myosin using the method of Margossian and

503 Lowey (85) with the modifications of Eads et al. (86). Purity of S1 was assessed by SDS-

504 PAGE, and the protein concentration was determined using the Bradford reagent

505 (Thermo Scientific). Porcine cardiac actin was purified from acetone powder (87) and

506 labeled with N-(1-pyrenyl)iodoacetamide (pyrene) as described previously (88, 89). Actin

507 concentrations were determined by absorbance at 290 nm (and 344 nm for pyrene-

508 labeled actin).

509

510 <u>Preparation of recombinant human cardiac tropomyosin and troponin</u>

511 pET3d vectors containing human cardiac tropomyosin, troponin-I, troponin-T, and

512 troponin-C were a generous gift from L. Tobacmann (University of Illinois at Chicago).

513 The ΔK210 mutation was introduced into troponin-T using a QuickChange Site-Directed

514 Mutagenesis Kit (Agilent) and verified by sequencing. Human cardiac troponin complex

515 subunits were expressed in *E. coli* and purified from BL21-CodonPlus (Agilent) using

516 established protocols (90), with the modification that the final protein was purified over a

517 MonoQ column (GE Healthcare) instead of a ResourceQ column. Troponin complex

518 concentration was measured using the Bradford reagent. Recombinant human

519 tropomyosin was purified from BL21-CodonPlus (Agilent) using established protocols (91)

520 with the modifications of McIntosh et al. (92). Tropomyosin concentration was determined

25

521   using absorbance at 280 nm. Before use in biochemical assays, tropomyosin was

522   reduced in 50 mM DTT at 56 °C for 5 minutes, and then aggregates were removed by

523   ultracentrifugation (92).

524

525   *In vitro* motility assay

526   *In vitro* motility assays were conducted as previously described (36). Phalloidin-stabilized

527   F-actin and rhodamine-phalloidin-stabilized F-actin were each prepared in KMg25 buffer

528   (25 mM KCl, 2 mM EGTA, 60 mM MOPS, 1 mM DTT, and 4 mM free $MgCl_2$). To remove

529   myosin dead-heads, full-length cardiac myosin in high salt buffer (KMg25 with 300 mM

530   KCl) with 2.17 µM phalloidin-stabilized F-actin and 1 mM ATP was sedimented at 355040

531   x g for 30 minutes at 4°C. A Bradford assay was used to determine the concentration of

532   functional myosin heads following sedimentation. Flow cells were assembled with two

533   glass coverslips (one coated with nitrocellulose) using double stick tape and vacuum

534   grease. One volume of myosin (200 nM) was added to the flow cell followed by 1 volume

535   of 1 mg/mL BSA, 1 volume unlabeled actin, 2 volumes of KMg25 + 1 mM ATP, 4 volumes

536   of KMg25, and then 1 volume of reconstituted thin filaments (40 nM rhodamine-phalloidin-

537   labeled actin with 2 µM troponin and tropomyosin). One volume equals 50 µL, which is

538   slightly larger than the flow cell volume. Activation of motility was initiated by adding 2

539   volumes of activation buffer (KMg25 with 4 mM ATP, 1 mg/mL glucose, 192 U/mL glucose

540   oxidase, 48 µg/mL catalase, 2 µM troponin and tropomyosin, 0.5% methyl cellulose). The

541   speed of thin filament translocation was recorded at room temperature (~20 °C) over 20

542   frames. 25 consistently moving filaments from each video were manually tracked and

26

543   analyzed using the MTrackJ plugin on Fiji ImageJ (93). Data were collected from 3

544   separate experiments.

545

546   Stopped-flow transient kinetics to determine K_B and the rate of ADP release

547   To determine K_B, the rate of myosin binding to regulated thin filaments was measured at

548   20 °C using stopped-flow techniques (47) in an SX-20 apparatus (Applied Photophysics).

549   Pyrene-actin was excited at 365 nm, and fluorescence emission was detected using a

550   395 nm long-pass filter. 5 µM phalloidin-stabilized pyrene actin, 2 µM tropomyosin, 2 µM

551   troponin, and 0.04 U/mL apyrase were rapidly mixed with 0.5 µM S1 myosin and 0.04

552   U/mL apyrase. The high calcium (pCa 4) buffer contained 200 mM KCl, 5mM $MgCl_2$, 60

553   mM MOPS, 2 mM EGTA, 1mM DTT, and 2.15 mM $CaCl_2$. The low calcium (pCa 9) buffer

554   contained 200 mM KCl, 5mM $MgCl_2$, 60 mM MOPS, 2 mM EGTA, 1 mM DTT and 5.2 µM

555    $CaCl_2$. Each experiment was the average of at least 3 separate mixes, and the data were

556   fit by a single exponential curve. K_B was calculated by using Equation 1. The average K_B

557   was calculated from three different experiments and the p-value was calculated using a

558   2-tailed Student's t-test.

559   The rate of ADP release from myosin bound to regulated thin filaments at 20 °C was

560   determined using stopped-flow techniques (94). 1 µM phalloidin-stabilized pyrene-actin,

561   1 µM S1 myosin, 100 µM ADP, 100 µM $MgCl_2$, 2 µM tropomyosin, and 2 µM troponin

562   were rapidly mixed with 5 mM ATP and 5 mM $MgCl_2$. The experiment was performed in

563   high calcium (pCa 4) buffer containing 25 mM KCl, 5mM $MgCl_2$, 60 mM MOPS, 2 mM

564   EGTA, 1 mM DTT, and 2.15 mM $CaCl_2$. The rate of ADP release was calculated by fitting

565   a single exponential function to the data, as we have previously done (89) (Figure 1 –

566   figure supplement 1). The average of three experiments was calculated, and statistical

567   testing was done using a two-tailed Student's t-test.

568

569   Fluorescence titrations to determine the values of K_W, K_T, and n

570   Fluorescence titrations were carried out at 20 °C as described in (47) to determine the

571   values of K_W, K_T, and n. S1 myosin (up to a final concentration of 10 μM) was added at

572   1-minute intervals to a stirred cuvette containing 0.5 μM pyrene-actin and 0.27 μM

573   troponin and tropomyosin. Titrations were performed at low (2 mM EGTA), intermediate

574   (pCa 6.25) and high (pCa 3) calcium concentrations. The buffers contained 200 mM KCl,

575   5 mM free $MgCl_2$, 60 mM MOPS, 2 mM EGTA, 1 mM DTT, 2 mM ADP, and the desired

576   free concentration of calcium from $CaCl_2$. The buffer also contained 50 μM

577   P1,P5-di(adenosine-5')pentaphosphate (Ap5A), 2 mM glucose, and 1 μM hexokinase to

578   eliminate any contaminating ATP. Five repeats were performed for each condition.

579   Titration curves were globally fit using an annealing algorithm in MATLAB (MathWorks)

580   (50). 95% confidence intervals were determined by fitting 1000 bootstrap simulations. A

581   test statistic was defined by calculating the difference in fit parameters between bootstrap

582   simulations of the WT and mutant data, and the p-value was determined from the fraction

583   of test statistic simulations that did not include the null hypothesis (i.e., that the

584   parameters for the WT are the same as the mutant). The fraction of thin filament in each

585   equilibrium state (Figure 3B) was calculated using the partition function.

586

587   Simulations

28

588   Simulations of force production by sarcomeres were conducted using the model

589   developed by Campbell et al. (52). This model enables the calculation of the normalized

590   force-pCa curve and the twitch force in response to a calcium transient for a given set of

591   equilibrium constants. Code for the simulation was kindly provided by Stuart Campbell.

592   For simulation of the WT protein, the default parameters were used, except the value of

593   the forward rate constant out of the blocked state was adjusted to equal 0.3 to capture

594   the measured value of K_B. This same K_B value was used for the mutant simulation, since

595   K_B was unchanged in the mutant. To simulate the mutant, the forward rate constant from

596   the closed to open state was set to 8.35 so that the equilibrium constant would be

597   proportional to the measured K_T.

598

599   Stem cell line derivation

600   The parent stem cell line, BJFF.6, was generated from the human BJ fibroblast

601   line (CRL-2522, ATCC) by the Genome Engineering and iPSC Center (GEiC) at

602   Washington University in St. Louis. hPSC reprogramming was done using the CytoTune-

603   iPS 2.0 Sendai reprogramming kit (A16517, ThermoFisher) following the manufacturer's

604   recommended protocol.

605

606   Whole exome sequencing

607   Whole exome sequencing of the BJFF stem cell line was performed by the

608   McDonnell Genome Institute (Washington University in St. Louis). DNA was isolated from

609   a frozen cell pellet using the QiaAMP DNA Mini Kit (Qiagen) according to the

29

610   manufacturer's recommendations. DNA was quantified fluorometrically using the Qubit

611   and dsDNA HS Assay kit (Invitrogen). The DNA yield was 22 µg / 5 million cells.

612   An automated dual-indexed library was constructed with 250 ng of genomic DNA

613   utilizing the KAPA HTP Library Kit (KAPA Biosystems) on the SciClone NGS instrument

614   (Perkin Elmer) targeting 250 bp inserts. 1 µg of library was hybridized with the xGen

615   Exome Research Panel v1.0 reagent (IDT Technologies) that spans 39 Mb target regions

616   (19,396 genes) of the human genome. The concentration of the captured library pool was

617   accurately determined through qPCR (Kapa Biosystems) to produce cluster counts

618   appropriate for the S2 flow cell on the NovaSeq platform (Illumina). A 2 x 151 base pair

619   end sequence data generated approximately 15 Gb per sample which led to greater than

620   90% of the targets covered at a minimum of 20x depth of coverage. The mean depth of

621   coverage was approximately 200x. Variants were identified using the Variant Effect

622   Predictor. Variants in genes that have been associated with cardiomyopathies (ABCC9,

623   ACTC1, ACTN2, ALMS1, ALPK3, ANKRD1, BAG3, BRAF, CAV3, CHRM2, CRYAB,

624   CSRP3, DES, DMD, DOLK, DSC2, DSG2, DSP, DTNA, EMD, FHL1, FKRP, FKTN,

625   FLNC, GATAD1, GLA, HCN4, HRAS, ILK, JPH2, JUP, KRAS, LAMA4, LAMP2, LDB3,

626   LMNA, MAP2K1, MAP2K2, MIB1, MTND1, MTND5, MTND6, MTTD, MTTG, MTTH,

627   MTTI, MTTK, MTTL1, MTTL2, MTTM, MTTQ, MTTS1, MTTS2, MURC, MYBPC3, MYH6,

628   MYH7, MYL2, MYL3, MYLK2, MYOZ2, MYPN, NEBL, NEXN, NKX2-5, NRAS, PDLIM3,

629   PKP2, PLN, PRDM16, PRKAG2, PTPN11, RAF1, RBM20, RIT1, RYR2, SCN5A, SGCD,

630   SOS1, TAZ, TCAP, TGFB3, TMEM43, TMPO, TNNC1, TNNI3, TNNT2, TPM1, TTN,

631   TTR, TXNRD2, VCL) were cross referenced with the ClinVar database. None of the

632   variants identified in the BJFF cell line have been characterized as pathogenic or likely

633   pathogenic in patients (Figure 5 – figure supplement 1).

634

635   <u>Derivation of the ΔK210 stem cell lines</u>

636   Two independent stem cell lines homozygous for the ΔK210 deletion, AN184.2-

637   hTNNT2, were generated from the BJFF.6 human hPSC line by Genome Engineering

638   and iPSC Center (GEiC) at Washington University in St. Louis using the CRISPR/Cas9

639   system (17, 95). The oligo used to generate the gRNA was

640   ACACCGAGAAGATTCTGGCTGAGAGGG (Figure 5 – figure supplement 2). This gRNA

641   was selected to minimize potential off-target effects based on an analysis of similar

642   sequences. The mutation was introduced using homology-directed repair to a single-

643   stranded oligodeoxynucleotide template (ssODN) with the deletion. Approximately 1 to

644   1.5×10^6 hPSCs were washed in DPBS and resuspended in P3 primary buffer (Lonza)

645   with 1 μg gRNA, 1.5 μg Cas9 vectors, and 1 μL ssODN (4μg, IDT) and then

646   electroporated with a 4D-Nucleofector (Lonza) using the CA-137 program. Following

647   nucleofection, cells were single-cell sorted (96) and screened with targeted deep

648   sequencing analysis (97) using primer sets specific to target regions. The ΔK210 deletion

649   was found in ~10% of the clones. Two clones with the ΔK210 mutation were then used

650   for all cellular experiments.

651   After gene editing, karyotype (G-banding) analysis was performed by Cell Line

652   Genetics. Cytogenetic analysis was performed on 20 G-banded metaphase cells (Cell

653   Line Genetics) and these cells had normal karyotypes (Figure 5 – figure supplement 3).

654   Cells were tested for myoplasma infections by the Genome Engineering core.

655   Pluripotency of gene-edited hPSCs was characterized by staining for SSEA4, OCT4,

656   SOX2, and TRA-1-61 using the Pluripotent Stem Cell 4-Marker Immunocytochemistry kit

657   (A25526, ThermoFisher) following the manufacturer's recommended protocol.

658   Immunofluorescent images of the stained cells were captured using a Nikon fluorescence

659   microscope and CCD camera. Cells showed robust staining for pluripotency markers

660   (Figure 5 – figure supplement 4).

661

662   Stem cell culture and differentiation to hPSC-CMs

663   All culture media contained 10 U/mL penicillin and 10 µg/mL streptomycin. hPSCs

664   were maintained at 37 °C and 5% CO_2 in feeder-free culture on Matrigel (Corning) coated

665   plates in Essential 8 Flex or StemFlex media (ThermoFisher). Cells were passaged using

666   0.02% EDTA (Sigma). After passaging, the E8 media was supplemented with 5 µM of the

667   ROCK inhibitor Y-27632 (Selleck Chem).

668   Differentiation to cardiomyocytes was accomplished using the method of Lian et

669   al. (53) (Figure 5 – figure supplement 5A). Briefly, hPSC colonies were dissociated to

670   single cells using Accutase (Gibco) and seeded into monolayers on 12-well Matrigel

671   coated plates at a density of 0.5-1 million cells per well. Cells were maintained in

672   StemFlex media supplemented with 5 µM Y-27632 for the first 24 hours. Two days after

673   seeding (day 0), the media was changed to RPMI/B27-I (RPMI-1640 media (Sigma)

674   containing B-27 supplement without insulin (ThermoFisher). 6-8 µM of the WNT agonist

675   CHIR-99021 (Selleck Chem) was added to initiate differentiation for 24 hours along with

676   1 µg/mL insulin to improve cell survival. On day 1, the WNT agonist was removed and

677   cells were cultured in RPMI/B27-I. On day 3, the media was collected and centrifuged to

678   remove debris. The conditioned media was combined with fresh RPMI/B27-I media in a

679   1:1 ratio and was supplemented with 5 µM of the WNT inhibitor IWP-2. On day 5, the

680   IWP2 was removed and the cells were cultured in RPMI/B27-I. On day 7, the media was

681   changed to RPMI/B27+I (RPMI-1640 media containing B-27 supplement with insulin) and

682   changed every 3 days. Spontaneous beating began on day 9-12.

683   To enrich the population of cardiomyocytes, metabolic selection was used (98).

684   On days 12-17, the cells were cultured in glucose-free media (glucose-free RPMI-1640

685   supplemented with B-27 supplement with insulin). On day 19, the cells were dissociated

686   using 0.25% trypsin and then passaged to gelatin coated culture dishes in RPMI-20

687   (RPMI-1640 + 20% FBS) with the addition of 10 µM Y-27632. Starting on day 21, cells

688   were cultured in RPMI/B27+I and the media was changed every 3 days. Metabolic

689   selection gave populations of >90% cardiomyocytes (Figure 5 -figure supplement 5B).

690   Cells were aged to at least day 30 after differentiation before being used for assays.

691

692   <u>Fabrication of stamps for microcontact patterning</u>

693   Stamps for microcontact printing were generated using standard microfabrication

694   techniques, based on the procedure in Ribeiro et al. (21). A photomask containing an

695   array of 17 x 118 µm (total area of 2000 µm^2) was generated (CAD/Art Services). SU-8-

696   3010 (Microchem) was spin coated on to a 3" silicon wafer (University Wafer) using a

697   Brewer Science CEE 200X instrument (Washington University Institute of Material

698   Sciences and Engineering) to generate a 15 µm thick layer. The wafer was then soft

699   baked at 65 °C for 90 seconds followed by 6 minutes at 95 °C. The mask exposure was

700   done using a Karl Suss MJB 3UV 400 Mask Aligner for a total exposure energy of 200

701   mJ/cm^2. Post exposure, the wafer was baked at 65 °C for 1 minute followed by 3 minutes

702   at 95 °C. The un-polymerized SU-8-3010 was then removed from the master by washing

703   in SU-8 developer (Y020100, Microchem).

704   Polydimethylsiloxane (PDMS) stamps for microcontact printing were prepared

705   from the SU-8 master. The SU-8 master was silanized using vapor deposition of

706   Trichloro(1H,1H,2H,2H-perfluoro-octyl) silane (Sigma) under vacuum. PDMS (Sylgard

707   184, Dow Corning) was prepared using a 10:1 w/w mixture of elastomer base:curing

708   agent. PDMS was degassed under vacuum, poured on the master, and cured overnight

709   under vacuum. The following day, the PDMS stamps were hard cured at 80 °C for 1 hour,

710   peeled from the master, and then cut into 18 x 18 mm squares using a razor blade.

711

712   Microcontact patterning of cardiomyocytes on glass

713   For patterning of cardiomyocytes on glass, glass coverslips were first cleaned by

714   sonication in isopropanol. The glass was washed twice with water and dried using

715   compressed nitrogen gas. The glass was then plasma cleaned under vacuum for 1

716   minute. The glass surface was passivated for 30 minutes in 0.1 mg/mL PLL-g-PEG

717   (SuSoS AG), then washed with water, and dried with nitrogen gas. PDMS stamps were

718   sterilized under UV light before use for at least 10 minutes. Geltrex (ThermoFisher) was

719   diluted 1:10 in DMEM-F12 and then 40 μL was added to the surface of the PDMS stamp

720   for 20 minutes. The Geltrex-coated PDMS stamp was dried with nitrogen gas and then

721   placed Geltrex side down on the PLL-g-PEG treated coverslip. A 50 or 100 g weight was

722   placed on top of the PDMS stamp for 2-3 minutes to transfer the Geltrex pattern onto the

34

723   coverslip. The stamped glass coverslips were then transferred to the bottom of a 6-well

724   tissue culture plate.

725   Cardiomyocytes were dissociated and singularized using 0.25% trypsin (Gibco).

726   Cells were resuspended in RPMI-20 with 10 µM Y-27632 at a density of 500 cells/µL and

727   then incubated on the patterned glass for 45 minutes. 18 mm coverslips required 300 µL

728   volume per coverslip. The patterned cardiomyocytes were cultured in RPMI-20 with Rock

729   inhibitor for 48 hours and were subsequently cultured in RPMI/B27+I with media changes

730   every 3 days.

731

732   Immunostaining and fluorescence microscopy

733   Cardiomyocytes were fixed for 15 minutes in 4% formaldehyde (Electron

734   Microscopy Sciences) in phosphate-buffered saline (PBS) and permeabilized with 0.1%

735   Triton X-100 (Sigma) for 20 minutes. The cells were blocked for 1 hour using a blocking

736   solution containing 3% bovine serum albumin (Gold Bio), 5% donkey serum (Sigma),

737   0.1% Triton X-100, and 0.02% sodium azide in PBS. Primary antibodies (see table below)

738   were added for 1 hour at room temperature or overnight at 4 °C. Cells were then washed

739   thoroughly in PBS before incubating for 1 hour in secondary antibody. Cells were again

740   thoroughly washed in PBS. For experiments with 4′,6-diamidino-2-phenylindole (DAPI),

741   the stain was used at a 1:50,000 dilution. For experiments using tetramethylrhodamine B

742   isothiocyanate labeled phalloidin, the phalloidin was added using a 1:1000 dilution. Cells

743   were visualized using a Nikon A1Rsi confocal microscope or a Nikon spinning disk

744   confocal microscope equipped with a Yokagawa CSU-X1 variable speed Nipkow spinning

745   disk scan head and an Andor Zyla 4.2 Megapixel sCMOS camera (Washington University

746   Center for Cellular Imaging). Z-stacks of cells with 60x magnification were recorded in

747   sequential scanning mode.

748

749   Antibodies used

Antibody	Product Number	Working Dilution	Host species	Vendor
Alpha-actinin	A7811/EA-53	1:500	mouse	Sigma
Troponin-I	SC-15368	1:300	rabbit	Santa Cruz
Cy3 anti-rabbit	711165152	1:300	donkey	Jackson Immuno.
Cy2 anti-mouse	715225150	1:300	donkey	Jackson Immuno.
OCT4	A25532	1:400	Rabbit	Invitrogen
SSEA4	A25530	1:100	Mouse	Invitrogen
SOX2	A24759	1:100	Rat	Invitrogen
TRA-1-60	A24868	1:100	Mouse	Invitrogen

750

751

752   Analysis of immunofluorescence images

753   Analysis of the organization of the sarcomeres was analyzed using software

754   developed by the Parker lab (55). Standard deviation projections were generated from Z-

755   stacks of hPSC-CMs stained for alpha-actinin. Data were pre-processed in FIJI/ImageJ

756   (93) using an ImageJ plugin (55). Data were then analyzed using the Parker software to

757   extract the orientational order parameter (OOP, a measure of sarcomeric alignment along

758   a single axis) (55). The cellular area, length, and width were calculated from thresholded

759   images of cardiomyocytes in ImageJ. Cumulative distributions of parameters were

760   generated in MATLAB (MathWorks). A Kruskal–Wallis one-way analysis of variance test

761   was used to compare the distributions. To compare individual parameters, 95%

36

762   confidence intervals were determined by calculating the mean parameter value from 1000

763   bootstrap simulations. A test statistic was defined by calculating the difference in fit

764   parameters between bootstrap simulations of the WT and mutant data, and the p-value

765   was determined from the fraction of test statistic simulations that did not include the null

766   hypothesis (i.e., that the parameters for the WT are the same as the mutant).

767

768   <u>Device fabrication for traction force microscopy</u>

769   Hydrogels for traction force microscopy were generated in 35 mm dishes according

770   to the protocol of Ribeiro et al., (21). The 14 mm glass-bottom of the 35 mm tissue culture

771   dishes (MatTek) were silanized with 0.4% 3-trimethoxylyl-propylmethacrylate (Sigma) for

772   1 hour and then washed with water and dried with nitrogen gas. To make 10 kPa

773   polyacrylamide hydrogels, a prepolymer solution containing 0.1% bisacrylamide was

774   used (99). 0.2 µm diameter fluorescent beads were added to the prepolymer solution

775   (FSSY002, Bangs Beads) as markers for the traction force.

776   Patterned coverslips were prepared using PDMS stamps and microcontact

777   printing. 12mm round coverslips were cleaned by plasma cleaning under vacuum for 5

778   minutes. 1:10 dilution of Geltrex was prepared in DMEM-F12. 40 µL of Geltrex was added

779   to the surface of the PDMS stamp and allowed to incubate for 20 minutes. Then the stamp

780   was dried with nitrogen gas and placed on the 12 mm round coverglass for 2-3 minutes

781   under a 50 g or 100 g weight, transferring the pattern to the coverglass. Unpatterned

782   coverslips were prepared by coating the entire surface of a 12 mm coverglass with

783   Geltrex.

784   To assemble the hydrogels, 15 µL of prepolymer solution was added to the

785   silanized glass tissue culture dishes and then the 12 mm Geltrex-patterned coverglass

786   was placed pattern side down. Hydrogels were allowed to polymerize for 15 minutes and

787   then PBS was added for at least 1 hour to hydrate the hydrogels. Hydrogels could also

788   be stored in PBS at 4°C until cell seeding. Before cell seeding, the 12 mm coverglass was

789   removed using forceps.

790

791   <u>Traction force microscopy</u>

792   All traction force microscopy measurements were performed on patterned

793   polyacrylamide hydrogels with a stiffness of 10 kPa with cardiomyocytes that were at least

794   30 days post-differentiation. Cardiomyocytes were singularized using 0.25% trypsin and

795   then resuspended in RPMI-20 with 10 µM Y-27632. PBS from the hydrogels was

796   aspirated and 100 µL of media containing 50,000 cells was added to the hydrogel surface.

797   After 45 minutes, 2 mL of RPMI-20 with 10 µM Y-27632 was added to the well. Cells were

798   placed in the incubator for 48 hours, and then the media was changed to RPMI/B27+I

799   and changed every 3 days until imaging.

800   On the day of imaging, fresh RPMI/B27+I was added 1 hour before imaging.

801   Single, spontaneously-beating cells were imaged in an environmentally controlled

802   chamber (Tokai Hit) on a Nikon spinning disk confocal microscope equipped with a

803   Yokagawa CSU-X1 variable speed Nipkow spinning disk scan head and Andor Zyla 4.2

804   Megapixel sCMOS camera (Washington University Center for Cellular Imaging). Cells

805   were imaged over an 800x400 pixel region of interest using a 40x objective. 20 seconds

806   of data were collected at 33 frames per second. Both bright-field and fluorescence images

807   were recorded.

808

809   Analysis of traction force microscopy data

810   Traction force movies were analyzed by generating displacement maps of the

811   fluorescent beads using a MATLAB program developed by the Pruitt lab (56). The

812   program enables the measurement of several parameters, including the force and power

813   output of single cells. The average rates of force development and relaxation for each cell

814   were calculated by fitting the time courses of the force developed with single exponential

815   functions. Cumulative distributions of parameters were generated in MATLAB. A Kruskal–

816   Wallis one-way analysis of variance test was used to compare the distributions. To

817   compare individual parameters, 95% confidence intervals were determined by calculating

818   the mean parameter value from 1000 bootstrapped simulations. A test statistic was

819   defined by calculating the difference in fit parameters between bootstrapping simulations

820   of the WT and mutant data, and the p-value was determined from the fraction of test

821   statistic simulations that did not include the null hypothesis (i.e., that the parameters for

822   the WT are the same as the mutant).

823

824   Hydrogel fabrication for immunofluorescence microscopy

825   Hydrogels for immunofluorescence microscopy were generated on 12 mm glass

826   coverslips according to the protocol of Ribeiro et al., (21). 12mm glass coverslips were

827   silanized with 0.4% 3-trimethoxylyl-propylmethacrylate (Sigma) for 1 hour and then

828   washed with water and dried with nitrogen gas. To make 10 kPa polyacrylamide

829   hydrogels, a prepolymer solution containing 0.1% bisacrylamide was used (99).

830   Patterned coverslips were prepared using PDMS stamps and microcontact

831   printing. 12 mm round coverslips were cleaned by plasma cleaning under vacuum for 5

832   minutes. 1:10 dilution of Geltrex was prepared in DMEM-F12. 40 µL of Geltrex was added

833   to the surface of the PDMS stamp and allowed to incubate for 20 minutes. Then the stamp

834   was dried with nitrogen gas and placed on the 12 mm round coverglass for 2-3 minutes

835   under a 50 g or 100 g weight, transferring the pattern to the coverglass.

836   To assemble the hydrogels, 15 µL of prepolymer solution was added to the

837   silanized 12 mm coverglass and then the 12 mm Geltrex patterned coverglass was placed

838   pattern side down to create a sandwich between the two coverglasses. Hydrogels were

839   allowed to polymerize for 15 minutes and the sandwiches were transferred into a 24-well

840   tissue culture plate. PBS was added for at least 1 hour to hydrate the hydrogels.

841   Hydrogels could also be stored in PBS at 4 °C until cell seeding. Before cell seeding, the

842   top coverglass was removed using a razor blade, leaving behind the 12 mm coverglass

843   with the patterned hydrogel. Cell seeding and immunofluorescence preparation and

844   imaging were carried out in the same manner as described in the traction force

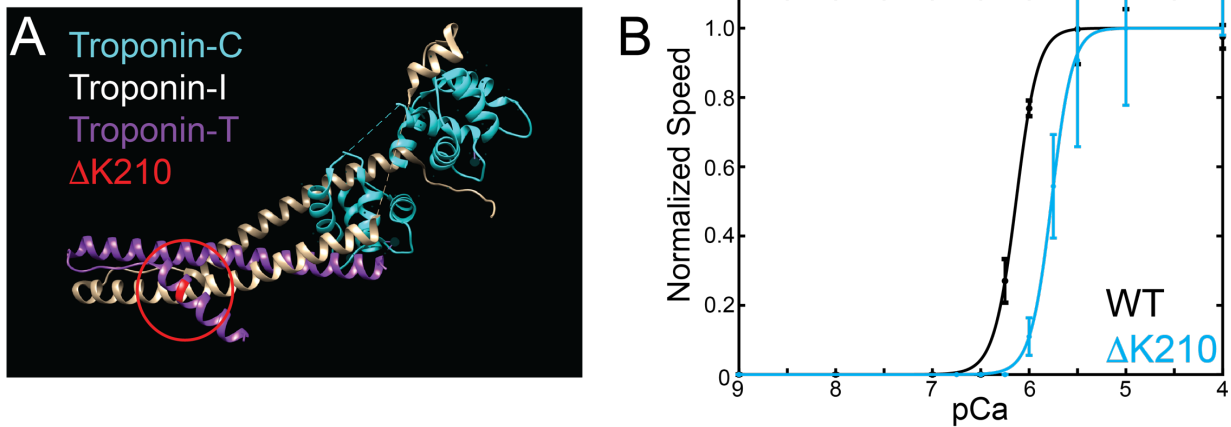845   microscopy and immunofluorescence sections above.

846

40

847

848 **Figure 1:** (A) Structure of the troponin core complex (PDB: 4Y99), showing troponin-C

849 (cyan), troponin-I (white), troponin-T (purple), and K210 of troponin-T (red). (B) Speed of

850 thin filament translocation as a function of calcium measured in the *in vitro* motility assay.

851 Error bars show the standard deviation of n=3 experiments. Data show a significant shift

852 in the pCa50 towards submaximal calcium activation for ΔK210 (p<0.0001). The Hill

853 coefficient is not changed between the WT and ΔK210 (p = 0.45).

854

855

856
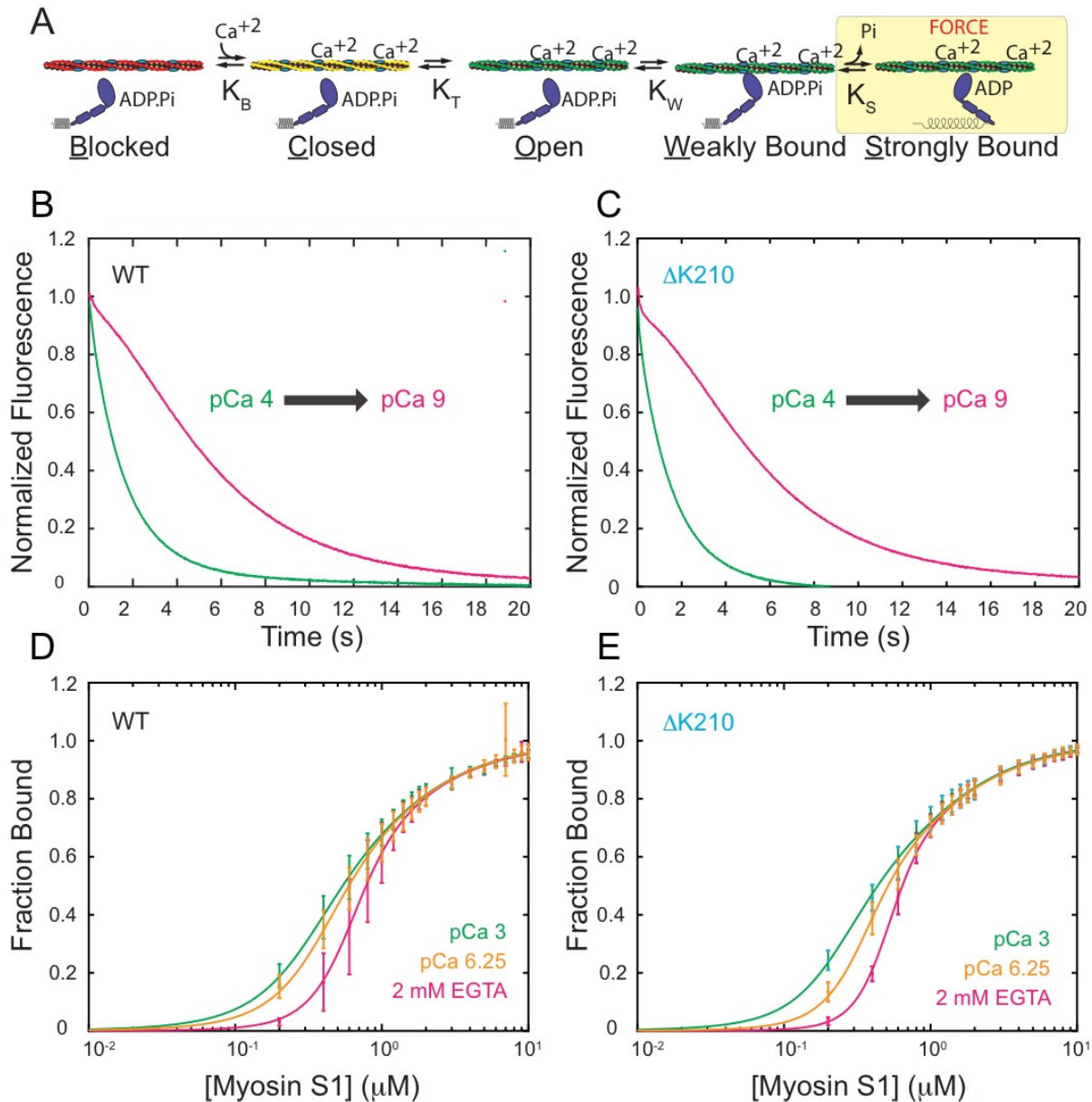
Figure 2: Determination of regulated thin filament parameters for ΔK210. (A) The three-state model for tropomyosin positioning along the thin filament (47). Activation of the thin filament and subsequent force generation requires both calcium and myosin binding. The equilibrium constant for the blocked to closed transition is K_B and the equilibrium constant for the closed to open transition is K_T. K_W and K_S are the equilibrium constants for myosin weak- and strong-binding to the thin filament, respectively. (B-C)

857
858
859
860
861
862

863   Normalized stopped-flow fluorescence traces of myosin binding to regulated pyrene-actin

864   binding. The quenching of pyrene-actin upon binding of S1 occurs at a faster rate at pCa

865   4 (green) compared to pCa 9 (pink) due to the activating effect of calcium. Traces for (A)

866   WT and (B) ΔK210 are very similar and the calculated values of K_B are not statistically

867   different (p=0.998). (D-E) Fluorescence titrations in which increasing amounts of S1

868   myosin were gradually added to regulated thin filaments to a final concentration of 10 μM

869   S1 in the presence of ADP. Titration curves at three different calcium concentrations are

870   shown for both (C) WT and (D) ΔK210. 5 repeats were performed for each condition. At

871   low concentrations of myosin, more myosin is bound to the thin filament at higher calcium

872   concentrations (pCa 6.25 (orange) and pCa 3 (green)) than at low calcium (2 mM EGTA,

873   pink).

874
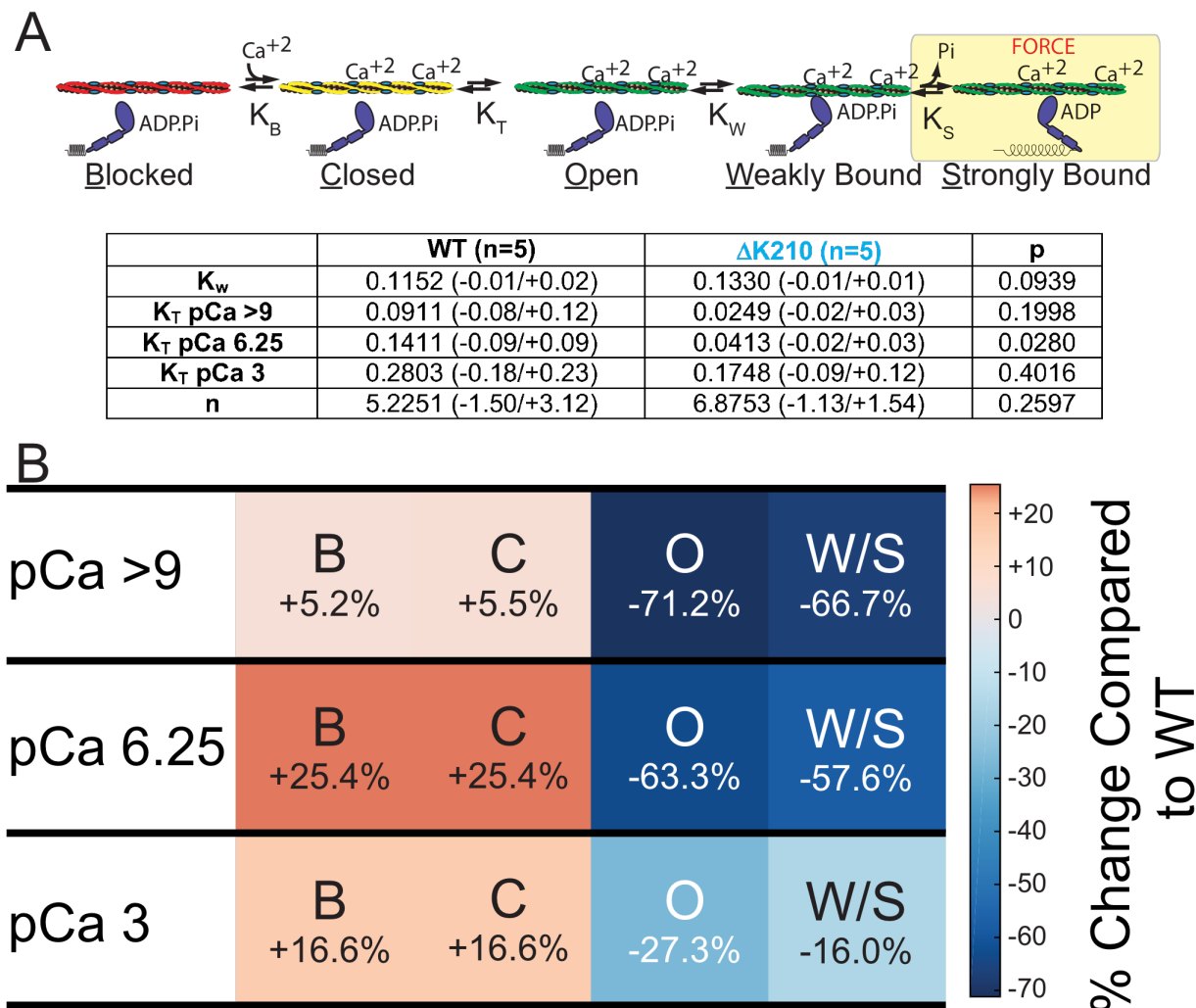
Figure 3: Effects of ΔK210 on tropomyosin positioning along the thin filament. (A) The three-state model for tropomyosin positioning along the thin filament (47) and parameter values obtained from the stopped-flow and fluorescence titration experiments. K_T for ΔK210 at pCa 6.25 is statistically different from WT (p=0.028). Error bars are the 95% confidence intervals. (B) Percent change in the occupancy of each state for the mutant compared to the WT. Reds denote increased population of a state, while blues denote decreased population. ΔK210 causes a decrease in the population of the states where myosin is bound to the thick filament and an increase in the population of the

884   inhibited (i.e., blocked and closed) states. Note that the change in the fractions in the

885   blocked and closed states is always the same, since K_B does not change between the
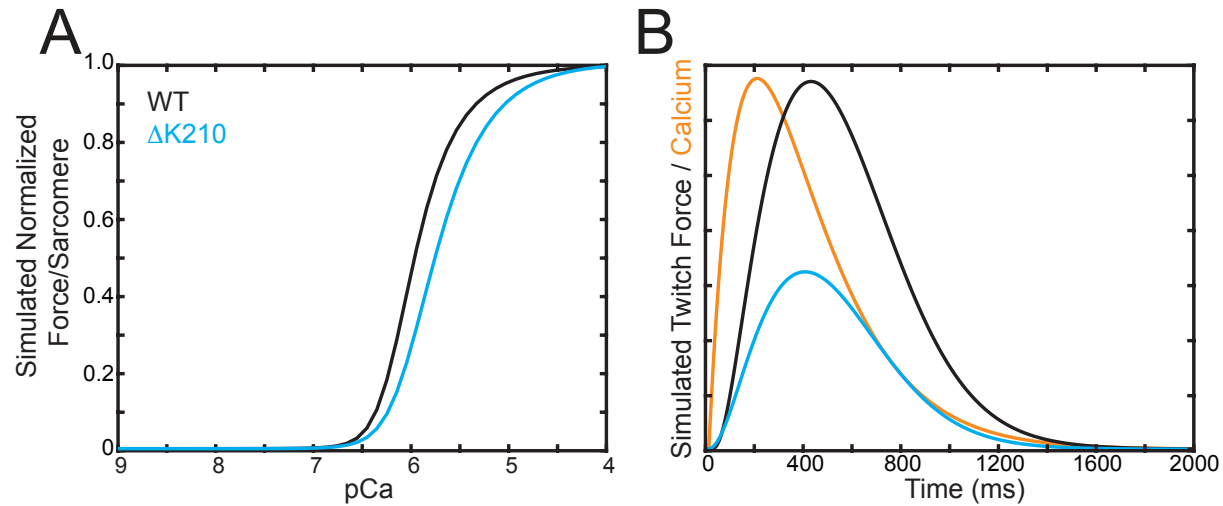
886   WT and the mutant.

887

888

889 **Figure 4: Computational modeling of the steady-state and transient force per**

890 **sarcomere.** (A) Using the model developed by Campbell et al. (52), the steady-state

891 normalized force per sarcomere can be simulated for both ΔK210 and WT. The simulation

892 shows a shift in the pCa50 towards supermaximal calcium activation in the mutant. (B)

893 Simulated twitch forces per sarcomere in response to a calcium transient. The model

894 predicts that ΔK210 should show a lower twitch force per sarcomere.

895

896
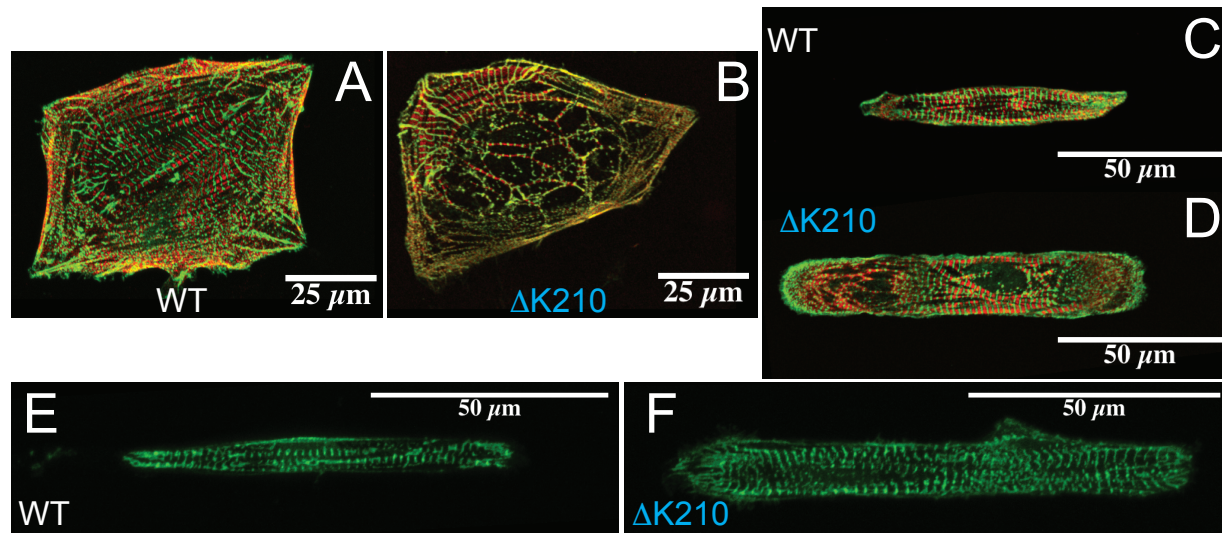
Figure 5: Immunofluorescence images of sarcomeres in hPSC-CMs. Troponin-I is

red and α-actinin is green. All images are z-projections. (A) WT hPSC-CM on glass. (B)

ΔK210 hPSC-CM on glass, showing sarcomeric disorganization. (C) WT cell on a

rectangular pattern on glass. (D) ΔK210 cell on a rectangular pattern on glass. (E) WT

cell on a rectangular pattern on a 10 kPa hydrogel. (F) ΔK210 cell on a rectangular pattern

on a 10 kPa hydrogel. The sarcomeric organization is significantly improved on the

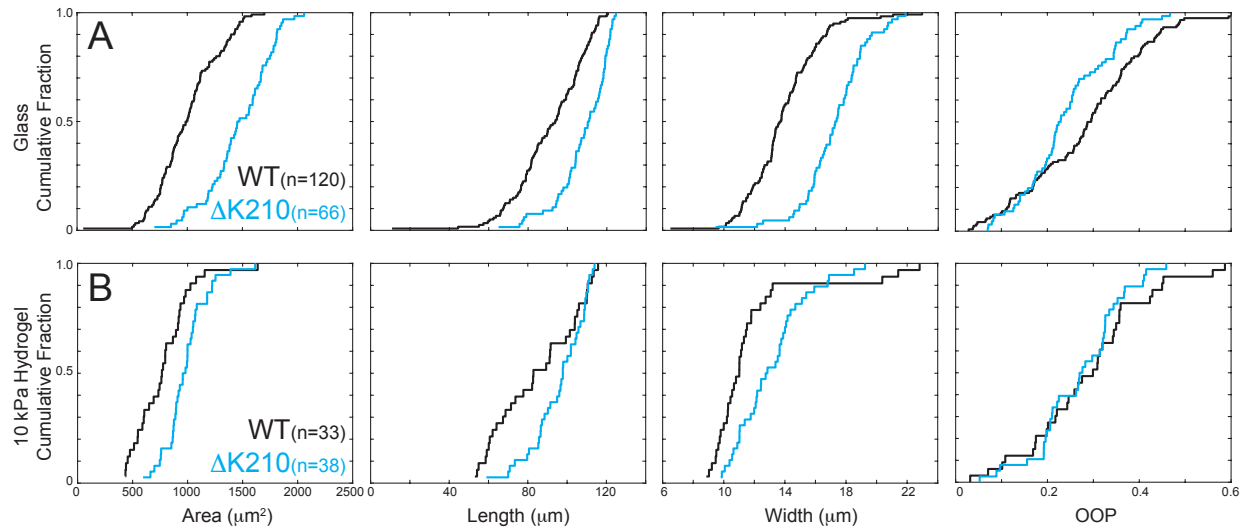hydrogel with physiologically relevant stiffness.

904

905

906

Figure 6: Quantification of immunofluorescence staining for sarcomeres in hPSC-CMs on rectangular patterns on (A) glass and (B) 10 kPa hydrogels. Data are plotted as cumulative distributions and parameter values can be found in Table 1. ΔK210 cells are significantly larger on both glass and 10 kPa hydrogels (p = 0.00002), due to increases in both length and width. The orientation order parameter (OOP) is a measurement of sarcomeric organization. For a hPSC-CM in which all of the sarcomeres are aligned along a single axis the OOP=1 and for a hPSC-CM with no preferred axis, the OOP = 0. On glass, ΔK210 cells have lower OOP values than the WT (p = 0.008). On physiological stiffness hydrogels, there is no significant difference between the OOP of the WT and mutant cells (p = 0.5).

907
908
909
910
911
912
913
914
915
916
917
918
919
920
921

48

922
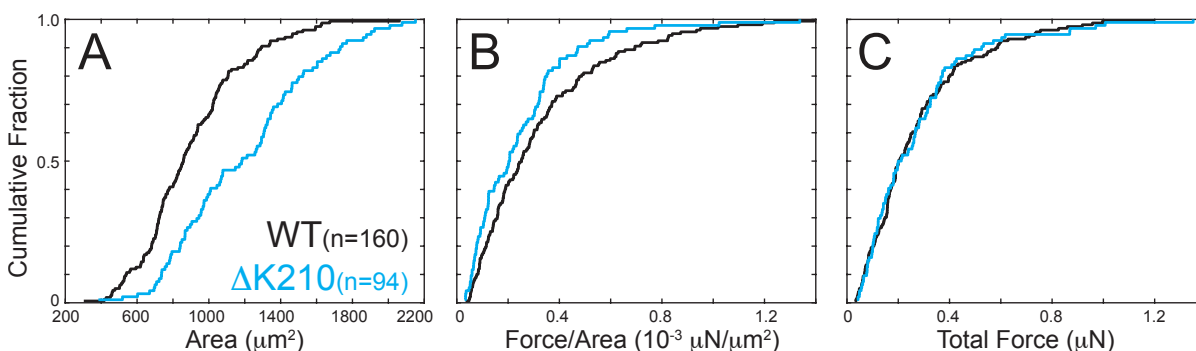
	WT (n=160)	ΔK210 (n=94)	p
Area (μm^2)	900 (-40/+50)	1200 (-80/+80)	<0.00002
Force / area (10^{-3} $\mu N/\mu m^2$)	0.32 (-0.04/+0.04)	0.25 (-0.04/+0.05)	0.01
Total force (μN)	0.27 (-0.03/+0.04)	0.27 (-0.04/+0.05)	0.98

923

924 **Figure 7: Traction force microscopy of single hPSC-CMs patterned on 10 kPa**

925 **polyacrylamide gels.** (A) Live ΔK210 hPSC-CMs on hydrogels are significantly larger

926 than WT cells. (B) ΔK210 cells have a lower force per area (i.e., force per sarcomere),

927 consistent with the molecular studies; however, since they are larger, (C) their total force

928 production is not significantly different from the WT cells.

Table 1: Analysis of Fixed Cell Sizes on Rectangular Patterns
Patterned on glass

	WT (n=120)	ΔK210 (n=66)	p
Area (μm^2)	1000 (-50/+50)	1470 (-70/+70)	0.00002
Length (μm)	91 (-3/+3)	108 (-3/+3)	0.00002
Width (μm)	13 (-0.4/+0.4)	17 (-0.5/+0.5)	0.00002
Length : width ratio	6.7 (-0.3/+0.3)	6.4 (-0.2/+0.3)	0.1
OOP	0.28 (-0.02/+0.02)	0.24 (-0.02/+0.02)	0.008

Patterned on 10 kPa hydrogels

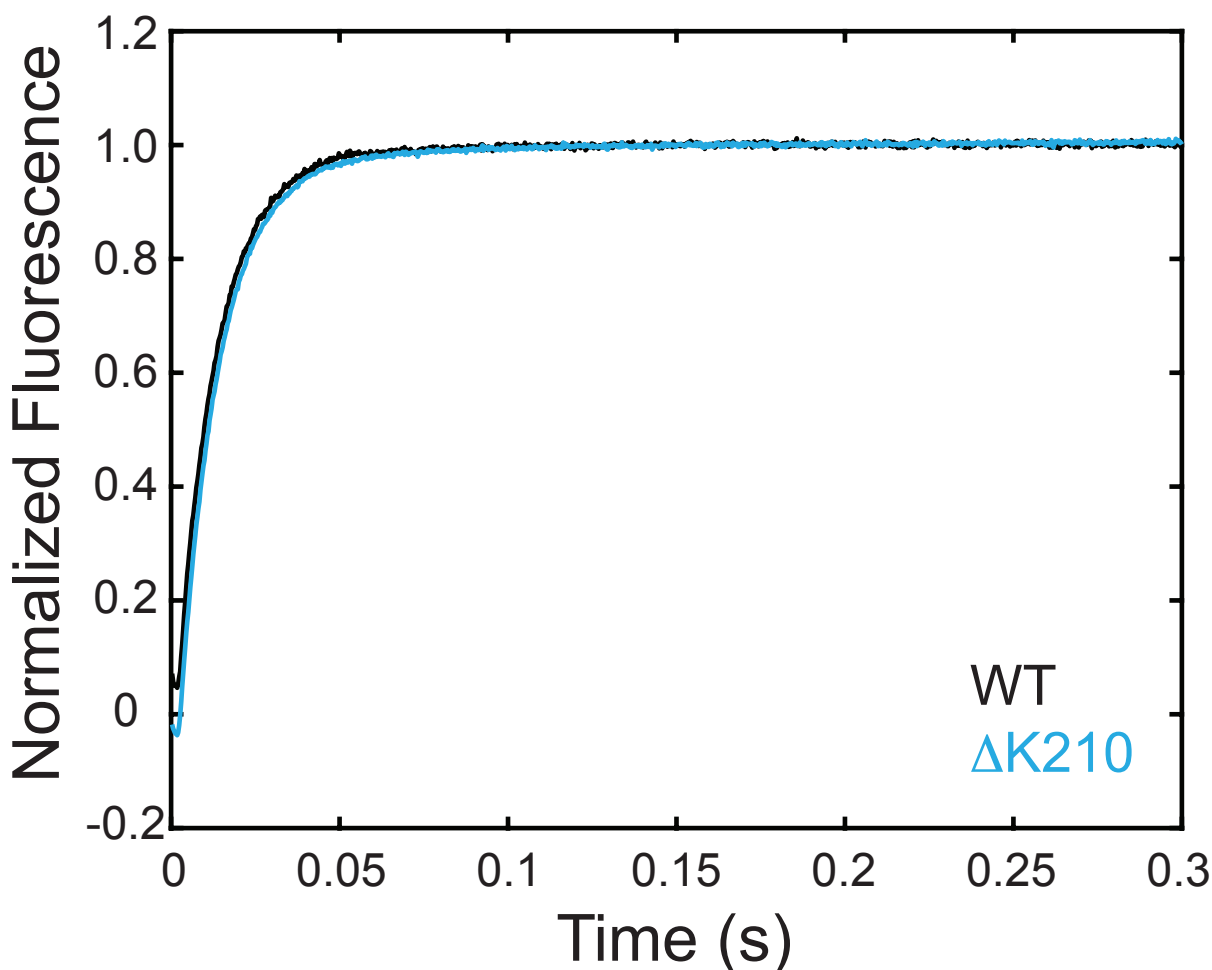|	WT (n=33)	ΔK210 (n=38)	p
Area (μm^2)	770 (-80/+90)	990 (-60/+60)	0.0002
Length (μm)	85 (-7/+7)	96 (-4/+4)	0.007
Width (μm)	11 (-1/+1)	13 (-0.7/+0.8)	0.06
Length : width ratio	7.6 (-0.9/+0.9)	7.6 (-0.6/+0.6)	0.9
OOP	0.28 (-0.04/+0.04)	0.27 (-0.03/+0.03)	0.5

929
930

50

931

932 **Figure 1 – figure supplement 1:** ADP release rates from myosin bound to regulated thin

933 filaments for WT and ΔK210 at 20°C. The data is the average of at least three individual

934 experiments. The ADP release rate in the presence of the mutation (72 s^{-1}) is not

935 significantly different from the WT (76 s^{-1}, p=0.344).

Chromosome	Position	ID	Gene	Change	CDS_position	Clinvar Annotation
1	78392446	rs1166698	NEXN	G/A	541	Benign
1	3328358	rs870124	PRDM16	C/C	1597	Benign
1	155880573	rs493446	RIT1	G/G	31	Benign
1	156107534	rs4641	LMNA	C/T	1698	Benign
2	73613031	rs61156725	ALMS1	T/T	36-41	Benign
2	179401740	rs55675869	TTN	C/T	73276	Benign
2	179411011	rs72648257	TTN	T/C	68227	Benign
2	179414992	rs72648244	TTN	T/C	64753	Benign
2	179421694	rs9808377	TTN	A/G	61367	Benign
2	179427536	rs3829746	TTN	T/C	56503	Benign
2	179431594	rs3731745	TTN	A/G	52445	Benign
2	179433221	rs56018860	TTN	T/C	50818	Benign
2	179433580	rs3813246	TTN	T/C	50459	Benign
2	179434139	rs3813245	TTN	A/G	49900	Benign
2	179437928	rs56201325	TTN	T/C	46111	Conflicting interpretations (benign (4) /likely benign (2) / unknown (1))
2	179444768	rs4145333	TTN	G/G	40426	Benign
2	179451420	rs2042996	TTN	G/A	37388	Benign
2	179464527	rs1001238	TTN	T/C	29281	Benign
2	179472292	rs2303832	TTN	T/A	26303	Benign
2	179498042	rs6723526	TTN	T/C	16138	Benign
2	179499530	rs2288563	TTN	T/C	15251	Benign
2	179518003	rs2562847	TTN	A/G	38753	Not found
2	179523514	rs200021871	TTN	T/A	37461	Benign
2	179528378	rs2163008	TTN	C/T	700	Benign
2	179554305	rs2244492	TTN	C/T	1498	Benign
2	179558366	rs2042995	TTN	T/C	1198	Benign
2	179581835	rs2562832	TTN	C/A	21894	Benign
2	179600648	rs2742347	TTN	C/T	10793	Benign
2	179604160	rs1883085	TTN	T/G	13086	Benign
2	179604366	rs2562829	TTN	T/G	12880	Benign
2	179606538	rs2627037	TTN	G/A	10708	Benign
2	179611711	rs66677602	TTN	C/A	15416	Benign
2	179615887	rs922984	TTN	T/C	11240	Benign
2	179615931	rs922985	TTN	G/G	11196	Benign
2	179621477	rs6433728	TTN	T/T	10213	Benign
2	179623758	rs2291310	TTN	C/T	10256	Benign
2	179629461	rs2291311	TTN	C/T	9781	Benign
2	179634936	rs2306636	TTN	C/T	8492	Benign
2	179637861	rs56142888	TTN	C/G	7830	Benign
2	179641975	rs12476289	TTN	C/T	4715	Benign
2	179644035	rs1552280	TTN	A/A	3884	Benign
2	179644855	rs10497520	TTN	T/C	3463	Benign
2	179658175	rs72647851	TTN	C/T	280	Benign
2	73716810	rs3820700	ALMS1	A/A	2555	Benign
2	73717103	rs2017116	ALMS1	C/C	2848	Benign
2	179582537	rs2627043	TTN	G/T	21332	Benign
2	179620951	rs7585334	TTN	C/T	10739	Benign
2	179444289	rs2288570	TTN	A/G	40815	Benign
4	186423637	rs4635850	PDLIM3	A/A	762	Benign
5	155935708	rs45559835	SGCD	G/A	287	Benign
6	7580285	rs138907450	DSP	A/C	3862	Likely benign (4) / unknown (4)
6	7581636	rs6929069	DSP	G/A	5213	Benign
6	112457383	rs1050349	LAMA4	G/C	3356	Benign
6	112457390	rs2032567	LAMA4	T/T	3349	Benign
6	112493872	rs1050348	LAMA4	A/G	1492	Benign
6	112508770	rs9400522	LAMA4	T/T	827	Benign
6	112471688	rs3734286	LAMA4	G/C	536	Not found
6	7576527	rs1016835	DSP	G/A	2631	Benign
9	108366734	rs34787999	FKTN	G/A	608	Benign
10	121429633	rs2234962	BAG3	C/C	277	Benign
10	69926334	rs10823148	MYPN	C/G	1884	Benign
10	69933921	rs10997975	MYPN	G/A	2072	Benign
10	69933969	rs7916821	MYPN	G/A	2120	Benign
10	69934258	rs3814182	MYPN	C/G	2409	Benign
10	69959242	rs7079481	MYPN	C/A	3403	Benign
10	112572458	rs1417635	RBM20	C/C	2303	Benign
10	112595719	rs942077	RBM20	C/C	3667	Benign
11	6630028	314683;rs7593	ILK	T/T	457	Not found
11	111781047	rs11603779	CRYAB	A/C	328	Benign
11	47371598	rs3729986	MYBPC3	C/T	472	Benign
12	21997457	rs182158174	ABCC9	A/C	3167	Not found
12	98927830	rs17459334	TMPO	C/G	1795	Benign
15	85401259	rs306197	ALPK3	C/T	3896	Benign
15	73660505	rs143090627	HCN4	C/T	107	Benign
17	39912145	rs1126821	JUP	A/A	2089	Benign
19	4102449	rs17851657	MAP2K2	G/A	162	Benign
22	19868218	rs1139793	TXNRD2	A/G	1040	Benign
22	19907099	rs5748469	TXNRD2	C/A	127	Benign
X	31496350	rs1800280	DMD	T/T	8810	Benign
X	31893307	rs1800275	DMD	G/G	7096	Benign

936

52

937 **Figure 5 – figure supplement 1: Variants identified from whole exome sequencing**

938 **of BJFF cells.** None of the identified variants in the BJFF line are classified as pathogenic

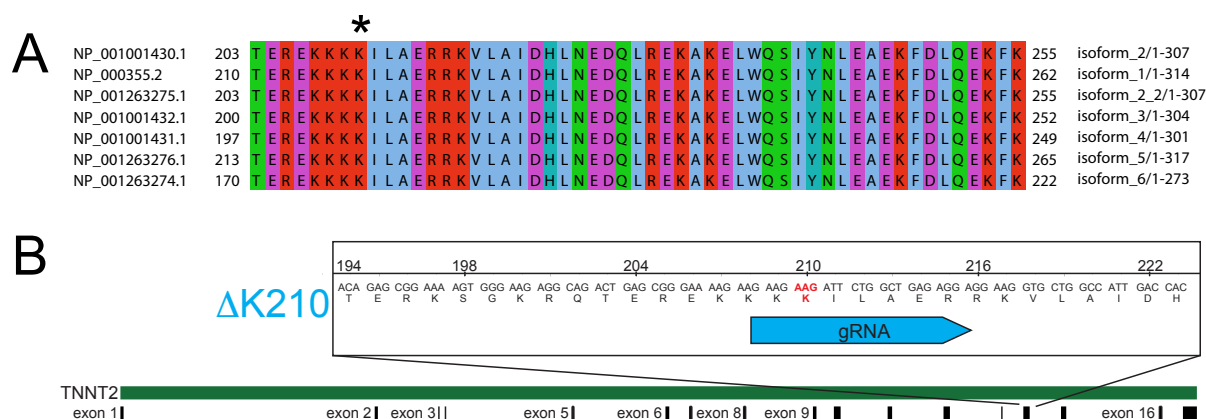939 or likely pathogenic in the ClinVar database.

940

941

942

943   **Figure 5 – figure supplement 2:** (A) Sequence alignment of all expressed human

944   TNNT2 splice isoforms. K210 (*) is located in a conserved region of the protein. (B)

945   CRISPR/Cas9 constructs for introducing the mutation into stem cells. This gRNA was

946   chosen to minimize the risk of potential off-target effects. The AAG deletion was

947   generated using a separate oligo for homology-directed repair, with an efficiency of ~10%.

948   Two homozygous clones positive for the mutation were validated using Next Generation

949   Sequencing.

950

951

54

952

953

Figure 5 – figure supplement 3: Karyotyping of gene edited cells. Cytogenetic analysis was performed on 20 G-banded metaphase cells (Cell Line Genetics) and these cells had normal karyotypes.
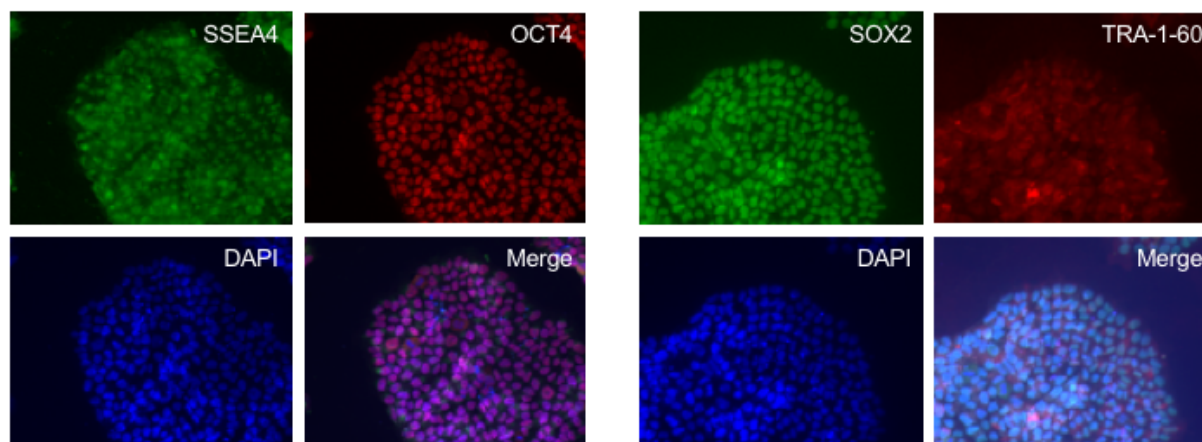
957

958

55

959

960

Figure 5 – figure supplement 4: Staining of gene-edited cells with markers of pluripotency demonstrates that stem cells retain pluripotency after gene editing.

963
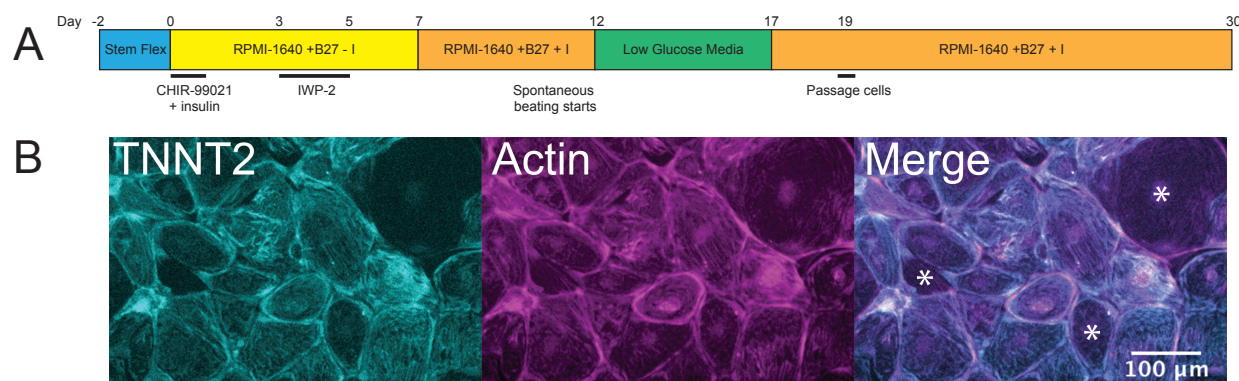
Figure 5 – figure supplement 5: (A) Differentiation protocol used. I indicates insulin. (B) Cardiomyocyte purity was assessed by immunofluorescence. Cells were stained 30 days after differentiation to assess cardiomyocyte purity. Cells were stained using an antibody for cardiac troponin-T (TNNT2, cyan) and phalloidin which labels actin and acts as a marker of all cells (magenta). Cells were imaged using epifluorescence illumination. Non-cardiomyocytes contained actin, but not TNNT2 (denoted with *). 711 cells were observed, 652 of which were cardiomyocytes. This gives a cardiomyocyte differentiation efficiency of 92%.

975 **References**

976 1. McNally, E. M., and L. Mestroni. 2017. Dilated Cardiomyopathy: Genetic Determinants
977 and Mechanisms. Circulation research 121:731-748.
978 2. Lynn, M. L., S. J. Lehman, and J. C. Tardiff. 2018. Biophysical Derangements in Genetic
979 Cardiomyopathies. Heart Fail Clin 14:147-159.
980 3. McNally, E. M., J. R. Golbus, and M. J. Puckelwartz. 2013. Genetic mutations and
981 mechanisms in dilated cardiomyopathy. The Journal of clinical investigation 123:19-26.
982 4. Spudich, J. A. 2014. Hypertrophic and dilated cardiomyopathy: four decades of basic
983 research on muscle lead to potential therapeutic approaches to these devastating genetic
984 diseases. Biophysical journal 106:1236-1249.
985 5. Williams, M. R., S. J. Lehman, J. C. Tardiff, and S. D. Schwartz. 2016. Atomic resolution
986 probe for allostery in the regulatory thin filament. Proceedings of the National Academy
987 of Sciences of the United States of America 113:3257-3262.
988 6. Hinson, J. T., A. Chopra, N. Nafissi, W. J. Polacheck, C. C. Benson, S. Swist, J. Gorham, L.
989 Yang, S. Schafer, C. C. Sheng, A. Haghighi, J. Homsy, N. Hubner, G. Church, S. A. Cook, W.
990 A. Linke, C. S. Chen, J. G. Seidman, and C. E. Seidman. 2015. HEART DISEASE. Titin
991 mutations in iPS cells define sarcomere insufficiency as a cause of dilated
992 cardiomyopathy. Science 349:982-986.
993 7. Lowey, S., V. Bretton, J. Gulick, J. Robbins, and K. M. Trybus. 2013. Transgenic mouse
994 alpha- and beta-cardiac myosins containing the R403Q mutation show isoform-
995 dependent transient kinetic differences. The Journal of biological chemistry 288:14780-
996 14787.
997 8. Ford, S. J., R. Mamidi, J. Jimenez, J. C. Tardiff, and M. Chandra. 2012. Effects of R92
998 mutations in mouse cardiac troponin T are influenced by changes in myosin heavy chain
999 isoform. Journal of molecular and cellular cardiology 53:542-551.
1000 9. Lowey, S., L. M. Lesko, A. S. Rovner, A. R. Hodges, S. L. White, R. B. Low, M. Rincon, J.
1001 Gulick, and J. Robbins. 2008. Functional effects of the hypertrophic cardiomyopathy
1002 R403Q mutation are different in an alpha- or beta-myosin heavy chain backbone. The
1003 Journal of biological chemistry 283:20579-20589.
1004 10. He, H., M. M. Javadpour, F. Latif, J. C. Tardiff, and J. S. Ingwall. 2007. R-92L and R-92W
1005 mutations in cardiac troponin T lead to distinct energetic phenotypes in intact mouse
1006 hearts. Biophysical journal 93:1834-1844.
1007 11. Roh, J., N. Houstis, and A. Rosenzweig. 2017. Why Don't We Have Proven Treatments for
1008 HFpEF? Circulation Research 120:1243.
1009 12. Conceição, G., I. Heinonen, A. P. Lourenço, D. J. Duncker, and I. Falcão-Pires. 2016. Animal
1010 models of heart failure with preserved ejection fraction. Netherlands Heart Journal
1011 24:275-286.
1012 13. Sacco, A., F. Mourkioti, R. Tran, J. Choi, M. Llewellyn, P. Kraft, M. Shkreli, S. Delp, J. H.
1013 Pomerantz, S. E. Artandi, and H. M. Blau. 2010. Short telomeres and stem cell exhaustion
1014 model Duchenne muscular dystrophy in mdx/mTR mice. Cell 143:1059-1071.
1015 14. Fananapazir, L., M. C. Dalakas, F. Cyran, G. Cohn, and N. D. Epstein. 1993. Missense
1016 mutations in the beta-myosin heavy-chain gene cause central core disease in

1017   hypertrophic cardiomyopathy. Proceedings of the National Academy of Sciences of the
1018   United States of America 90:3993-3997.
1019   15. Lian, X., C. Hsiao, G. Wilson, K. Zhu, L. B. Hazeltine, S. M. Azarin, K. K. Raval, J. Zhang, T. J.
1020   Kamp, and S. P. Palecek. 2012. Robust cardiomyocyte differentiation from human
1021   pluripotent stem cells via temporal modulation of canonical Wnt signaling. Proceedings
1022   of the National Academy of Sciences of the United States of America 109:E1848-1857.
1023   16. Kehat, I., D. Kenyagin-Karsenti, M. Snir, H. Segev, M. Amit, A. Gepstein, E. Livne, O. Binah,
1024   J. Itskovitz-Eldor, and L. Gepstein. 2001. Human embryonic stem cells can differentiate
1025   into myocytes with structural and functional properties of cardiomyocytes. The Journal
1026   of clinical investigation 108:407-414.
1027   17. Jinek, M., K. Chylinski, I. Fonfara, M. Hauer, J. A. Doudna, and E. Charpentier. 2012. A
1028   programmable dual-RNA-guided DNA endonuclease in adaptive bacterial immunity.
1029   Science 337:816-821.
1030   18. Sun, N., M. Yazawa, J. Liu, L. Han, V. Sanchez-Freire, O. J. Abilez, E. G. Navarrete, S. Hu, L.
1031   Wang, A. Lee, A. Pavlovic, S. Lin, R. Chen, R. J. Hajjar, M. P. Snyder, R. E. Dolmetsch, M. J.
1032   Butte, E. A. Ashley, M. T. Longaker, R. C. Robbins, and J. C. Wu. 2012. Patient-specific
1033   induced pluripotent stem cells as a model for familial dilated cardiomyopathy. Science
1034   translational medicine 4:130ra147.
1035   19. Lam, C. K., and J. C. Wu. 2018. Disease modelling and drug discovery for hypertrophic
1036   cardiomyopathy using pluripotent stem cells: how far have we come? Eur Heart J.
1037   20. Musunuru, K., F. Sheikh, R. M. Gupta, S. R. Houser, K. O. Maher, D. J. Milan, A. Terzic, J. C.
1038   Wu, G. American Heart Association Council on Functional, B. Translational, Y. Council on
1039   Cardiovascular Disease in the, C. Council on, and N. Stroke. 2018. Induced Pluripotent
1040   Stem Cells for Cardiovascular Disease Modeling and Precision Medicine: A Scientific
1041   Statement From the American Heart Association. Circ Genom Precis Med 11:e000043.
1042   21. Ribeiro, A. J., Y. S. Ang, J. D. Fu, R. N. Rivas, T. M. Mohamed, G. C. Higgs, D. Srivastava, and
1043   B. L. Pruitt. 2015. Contractility of single cardiomyocytes differentiated from pluripotent
1044   stem cells depends on physiological shape and substrate stiffness. Proceedings of the
1045   National Academy of Sciences of the United States of America 112:12705-12710.
1046   22. Feaster, T. K., A. G. Cadar, L. Wang, C. H. Williams, Y. W. Chun, J. E. Hempel, N.
1047   Bloodworth, W. D. Merryman, C. C. Lim, J. C. Wu, B. C. Knollmann, and C. C. Hong. 2015.
1048   Matrigel Mattress: A Method for the Generation of Single Contracting Human-Induced
1049   Pluripotent Stem Cell-Derived Cardiomyocytes. Circulation research 117:995-1000.
1050   23. Jiang, Y., P. Park, S. M. Hong, and K. Ban. 2018. Maturation of Cardiomyocytes Derived
1051   from Human Pluripotent Stem Cells: Current Strategies and Limitations. Mol Cells 41:613-
1052   621.
1053   24. Hershberger, R. E., J. R. Pinto, S. B. Parks, J. D. Kushner, D. Li, S. Ludwigsen, J. Cowan, A.
1054   Morales, M. S. Parvatiyar, and J. D. Potter. 2009. Clinical and functional characterization
1055   of TNNT2 mutations identified in patients with dilated cardiomyopathy. Circ Cardiovasc
1056   Genet 2:306-313.
1057   25. Mogensen, J., R. T. Murphy, T. Shaw, A. Bahl, C. Redwood, H. Watkins, M. Burke, P. M.
1058   Elliott, and W. J. McKenna. 2004. Severe disease expression of cardiac troponin C and T
1059   mutations in patients with idiopathic dilated cardiomyopathy. Journal of the American
1060   College of Cardiology 44:2033-2040.

1061 26. Kamisago, M., S. D. Sharma, S. R. DePalma, S. Solomon, P. Sharma, B. McDonough, L.
1062   Smoot, M. P. Mullen, P. K. Woolf, E. D. Wigle, J. G. Seidman, and C. E. Seidman. 2000.
1063   Mutations in sarcomere protein genes as a cause of dilated cardiomyopathy. The New
1064   England journal of medicine 343:1688-1696.
1065 27. Hanson, E. L., P. M. Jakobs, H. Keegan, K. Coates, S. Bousman, N. H. Dienel, M. Litt, and R.
1066   E. Hershberger. 2002. Cardiac troponin T lysine 210 deletion in a family with dilated
1067   cardiomyopathy. J Card Fail 8:28-32.
1068 28. Dewan, S., K. J. McCabe, M. Regnier, and A. D. McCulloch. 2017. Insights and Challenges
1069   of Multi-Scale Modeling of Sarcomere Mechanics in cTn and Tm DCM Mutants-Genotype
1070   to Cellular Phenotype. Front Physiol 8:151.
1071 29. Garfinkel, A. C., J. G. Seidman, and C. E. Seidman. 2018. Genetic Pathogenesis of
1072   Hypertrophic and Dilated Cardiomyopathy. Heart Fail Clin 14:139-146.
1073 30. Memo, M., M. C. Leung, D. G. Ward, C. Dos Remedios, S. Morimoto, L. Zhang, G.
1074   Ravenscroft, E. McNamara, K. J. Nowak, S. B. Marston, and A. E. Messer. 2013. Familial
1075   dilated cardiomyopathy mutations uncouple troponin I phosphorylation from changes in
1076   myofibrillar Ca2+ sensitivity. Cardiovascular research 99:65-73.
1077 31. Du, C. K., S. Morimoto, K. Nishii, R. Minakami, M. Ohta, N. Tadano, Q. W. Lu, Y. Y. Wang,
1078   D. Y. Zhan, M. Mochizuki, S. Kita, Y. Miwa, F. Takahashi-Yanaga, T. Iwamoto, I. Ohtsuki,
1079   and T. Sasaguri. 2007. Knock-in mouse model of dilated cardiomyopathy caused by
1080   troponin mutation. Circulation research 101:185-194.
1081 32. Lu, Q. W., S. Morimoto, K. Harada, C. K. Du, F. Takahashi-Yanaga, Y. Miwa, T. Sasaguri, and
1082   I. Ohtsuki. 2003. Cardiac troponin T mutation R141W found in dilated cardiomyopathy
1083   stabilizes the troponin T-tropomyosin interaction and causes a Ca2+ desensitization.
1084   Journal of molecular and cellular cardiology 35:1421-1427.
1085 33. Morimoto, S., Q. W. Lu, K. Harada, F. Takahashi-Yanaga, R. Minakami, M. Ohta, T.
1086   Sasaguri, and I. Ohtsuki. 2002. Ca(2+)-desensitizing effect of a deletion mutation Delta
1087   K210 in cardiac troponin T that causes familial dilated cardiomyopathy. Proceedings of
1088   the National Academy of Sciences of the United States of America 99:913-918.
1089 34. Ahmad, F., S. K. Banerjee, M. L. Lage, X. N. Huang, S. H. Smith, S. Saba, J. Rager, D. A.
1090   Conner, A. M. Janczewski, K. Tobita, J. P. Tinney, I. P. Moskowitz, A. R. Perez-Atayde, B. B.
1091   Keller, M. A. Mathier, S. G. Shroff, C. E. Seidman, and J. G. Seidman. 2008. The role of
1092   cardiac troponin T quantity and function in cardiac development and dilated
1093   cardiomyopathy. PloS one 3:e2642.
1094 35. Chandra, M., M. L. Tschirgi, S. J. Ford, B. K. Slinker, and K. B. Campbell. 2007. Interaction
1095   between myosin heavy chain and troponin isoforms modulate cardiac myofiber
1096   contractile dynamics. American journal of physiology. Regulatory, integrative and
1097   comparative physiology 293:R1595-1607.
1098 36. Greenberg, M. J., K. Kazmierczak, D. Szczesna-Cordary, and J. R. Moore. 2010.
1099   Cardiomyopathy-linked myosin regulatory light chain mutations disrupt myosin strain-
1100   dependent biochemistry. Proceedings of the National Academy of Sciences of the United
1101   States of America 107:17403-17408.
1102 37. Greenberg, M. J., J. D. Watt, M. Jones, K. Kazmierczak, D. Szczesna-Cordary, and J. R.
1103   Moore. 2009. Regulatory light chain mutations associated with cardiomyopathy affect
1104   myosin mechanics and kinetics. Journal of molecular and cellular cardiology 46:108-115.

60

1105   38.   Greenberg, M. J., H. Shuman, and E. M. Ostap. 2014. Inherent force-dependent properties
1106   of beta-cardiac myosin contribute to the force-velocity relationship of cardiac muscle.
1107   Biophysical journal 107:L41-44.
1108   39.   Sung, J., S. Nag, K. I. Mortensen, C. L. Vestergaard, S. Sutton, K. Ruppel, H. Flyvbjerg, and
1109   J. A. Spudich. 2015. Harmonic force spectroscopy measures load-dependent kinetics of
1110   individual human beta-cardiac myosin molecules. Nat Commun 6:7931.
1111   40.   Deacon, J. C., M. J. Bloemink, H. Rezavandi, M. A. Geeves, and L. A. Leinwand. 2012.
1112   Identification of functional differences between recombinant human alpha and beta
1113   cardiac myosin motors. Cellular and molecular life sciences : CMLS 69:2261-2277.
1114   41.   Woody, M. S., M. J. Greenberg, B. Barua, D. A. Winkelmann, Y. E. Goldman, and E. M.
1115   Ostap. 2018. Positive cardiac inotrope omecamtiv mecarbil activates muscle despite
1116   suppressing the myosin working stroke. Nat Commun 9:3838.
1117   42.   Kron, S. J., and J. A. Spudich. 1986. Fluorescent actin filaments move on myosin fixed to a
1118   glass surface. Proceedings of the National Academy of Sciences of the United States of
1119   America 83:6272-6276.
1120   43.   Homsher, E., B. Kim, A. Bobkova, and L. S. Tobacman. 1996. Calcium regulation of thin
1121   filament movement in an in vitro motility assay. Biophysical journal 70:1881-1892.
1122   44.   Robinson, P., M. Mirza, A. Knott, H. Abdulrazzak, R. Willott, S. Marston, H. Watkins, and
1123   C. Redwood. 2002. Alterations in thin filament regulation induced by a human cardiac
1124   troponin T mutant that causes dilated cardiomyopathy are distinct from those induced by
1125   troponin T mutants that cause hypertrophic cardiomyopathy. The Journal of biological
1126   chemistry 277:40710-40716.
1127   45.   Barany, M. 1967. ATPase activity of myosin correlated with speed of muscle shortening.
1128   The Journal of general physiology 50:Suppl:197-218.
1129   46.   Sommese, R. F., S. Nag, S. Sutton, S. M. Miller, J. A. Spudich, and K. M. Ruppel. 2013.
1130   Effects of troponin T cardiomyopathy mutations on the calcium sensitivity of the
1131   regulated thin filament and the actomyosin cross-bridge kinetics of human beta-cardiac
1132   myosin. PloS one 8:e83403.
1133   47.   McKillop, D. F., and M. A. Geeves. 1993. Regulation of the interaction between actin and
1134   myosin subfragment 1: evidence for three states of the thin filament. Biophysical journal
1135   65:693-701.
1136   48.   Lehman, W., R. Craig, and P. Vibert. 1994. Ca(2+)-induced tropomyosin movement in
1137   Limulus thin filaments revealed by three-dimensional reconstruction. Nature 368:65-67.
1138   49.   Vibert, P., R. Craig, and W. Lehman. 1997. Steric-model for activation of muscle thin
1139   filaments. Journal of molecular biology 266:8-14.
1140   50.   Barrick, S. K., S. R. Clippinger, L. Greenberg, and M. J. Greenberg. 2019. Computational
1141   Tool to Study Perturbations in Muscle Regulation and its Application to Heart Disease.
1142   Biorxiv.
1143   51.   Maytum, R., B. Westerdorf, K. Jaquet, and M. A. Geeves. 2003. Differential regulation of
1144   the actomyosin interaction by skeletal and cardiac troponin isoforms. The Journal of
1145   biological chemistry 278:6696-6701.
1146   52.   Campbell, S. G., F. V. Lionetti, K. S. Campbell, and A. D. McCulloch. 2010. Coupling of
1147   adjacent tropomyosins enhances cross-bridge-mediated cooperative activation in a
1148   markov model of the cardiac thin filament. Biophysical journal 98:2254-2264.

53. Lian, X., J. Zhang, S. M. Azarin, K. Zhu, L. B. Hazeltine, X. Bao, C. Hsiao, T. J. Kamp, and S. P. Palecek. 2013. Directed cardiomyocyte differentiation from human pluripotent stem cells by modulating Wnt/beta-catenin signaling under fully defined conditions. Nature protocols 8:162-175.

54. Chopra, A., M. L. Kutys, K. Zhang, W. J. Polacheck, C. C. Sheng, R. J. Luu, J. Eyckmans, J. T. Hinson, J. G. Seidman, C. E. Seidman, and C. S. Chen. 2018. Force Generation via beta-Cardiac Myosin, Titin, and alpha-Actinin Drives Cardiac Sarcomere Assembly from Cell-Matrix Adhesions. Developmental cell 44:87-96 e85.

55. Pasqualini, F. S., S. P. Sheehy, A. Agarwal, Y. Aratyn-Schaus, and K. K. Parker. 2015. Structural phenotyping of stem cell-derived cardiomyocytes. Stem Cell Reports 4:340-347.

56. Ribeiro, A. J. S., O. Schwab, M. A. Mandegar, Y. S. Ang, B. R. Conklin, D. Srivastava, and B. L. Pruitt. 2017. Multi-Imaging Method to Assay the Contractile Mechanical Output of Micropatterned Human iPSC-Derived Cardiac Myocytes. Circulation research 120:1572-1583.

57. Nag, S., R. F. Sommese, Z. Ujfalusi, A. Combs, S. Langer, S. Sutton, L. A. Leinwand, M. A. Geeves, K. M. Ruppel, and J. A. Spudich. 2015. Contractility parameters of human beta-cardiac myosin with the hypertrophic cardiomyopathy mutation R403Q show loss of motor function. Sci Adv 1:e1500511.

58. Tyska, M. J., E. Hayes, M. Giewat, C. E. Seidman, J. G. Seidman, and D. M. Warshaw. 2000. Single-molecule mechanics of R403Q cardiac myosin isolated from the mouse model of familial hypertrophic cardiomyopathy. Circulation research 86:737-744.

59. Palmiter, K. A., M. J. Tyska, J. R. Haeberle, N. R. Alpert, L. Fananapazir, and D. M. Warshaw. 2000. R403Q and L908V mutant beta-cardiac myosin from patients with familial hypertrophic cardiomyopathy exhibit enhanced mechanical performance at the single molecule level. Journal of muscle research and cell motility 21:609-620.

60. Greenberg, M. J., G. Arpag, E. Tuzel, and E. M. Ostap. 2016. A Perspective on the Role of Myosins as Mechanosensors. Biophysical journal 110:2568-2576.

61. Jin, J. P., and S. M. Chong. 2010. Localization of the two tropomyosin-binding sites of troponin T. Arch Biochem Biophys 500:144-150.

62. Sfichi-Duke, L., M. L. Garcia-Cazarin, C. A. Sumandea, G. A. Sievert, C. W. Balke, D. Y. Zhan, S. Morimoto, and M. P. Sumandea. 2010. Cardiomyopathy-causing deletion K210 in cardiac troponin T alters phosphorylation propensity of sarcomeric proteins. Journal of molecular and cellular cardiology 48:934-942.

63. Liu, B., S. B. Tikunova, K. P. Kline, J. K. Siddiqui, and J. P. Davis. 2012. Disease-related cardiac troponins alter thin filament Ca2+ association and dissociation rates. PloS one 7:e38259.

64. Houmeida, A., D. H. Heeley, B. Belknap, and H. D. White. 2010. Mechanism of regulation of native cardiac muscle thin filaments by rigor cardiac myosin-S1 and calcium. The Journal of biological chemistry 285:32760-32769.

65. Mijailovich, S. M., X. Li, J. C. del Alamo, R. H. Griffiths, V. Kecman, and M. A. Geeves. 2010. Resolution and uniqueness of estimated parameters of a model of thin filament regulation in solution. Computational biology and chemistry 34:19-33.

1192   66.   Smith, D. A., M. A. Geeves, J. Sleep, and S. M. Mijailovich. 2008. Towards a unified theory
1193   of muscle contraction. I: foundations. Ann Biomed Eng 36:1624-1640.
1194   67.   Longyear, T., S. Walcott, and E. P. Debold. 2017. The molecular basis of thin filament
1195   activation: from single molecule to muscle. Sci Rep 7:1822.
1196   68.   Hill, T. L., E. Eisenberg, and L. Greene. 1980. Theoretical model for the cooperative
1197   equilibrium binding of myosin subfragment 1 to the actin-troponin-tropomyosin complex.
1198   Proceedings of the National Academy of Sciences of the United States of America
1199   77:3186-3190.
1200   69.   Gomes, A. V., G. Guzman, J. Zhao, and J. D. Potter. 2002. Cardiac troponin T isoforms
1201   affect the Ca2+ sensitivity and inhibition of force development. Insights into the role of
1202   troponin T isoforms in the heart. The Journal of biological chemistry 277:35341-35349.
1203   70.   Iorga, B., K. Schwanke, N. Weber, M. Wendland, S. Greten, B. Piep, C. G. Dos Remedios,
1204   U. Martin, R. Zweigerdt, T. Kraft, and B. Brenner. 2017. Differences in Contractile Function
1205   of Myofibrils within Human Embryonic Stem Cell-Derived Cardiomyocytes vs. Adult
1206   Ventricular Myofibrils Are Related to Distinct Sarcomeric Protein Isoforms. Front Physiol
1207   8:1111.
1208   71.   Kadota, S., L. Pabon, H. Reinecke, and C. E. Murry. 2017. In Vivo Maturation of Human
1209   Induced Pluripotent Stem Cell-Derived Cardiomyocytes in Neonatal and Adult Rat Hearts.
1210   Stem Cell Reports 8:278-289.
1211   72.   Birket, M. J., M. C. Ribeiro, G. Kosmidis, D. Ward, A. R. Leitoguinho, V. van de Pol, C.
1212   Dambrot, H. D. Devalla, R. P. Davis, P. G. Mastroberardino, D. E. Atsma, R. Passier, and C.
1213   L. Mummery. 2015. Contractile Defect Caused by Mutation in MYBPC3 Revealed under
1214   Conditions Optimized for Human PSC-Cardiomyocyte Function. Cell Rep 13:733-745.
1215   73.   Forsey, J., L. Benson, E. Rozenblyum, M. K. Friedberg, and L. Mertens. 2014. Early changes
1216   in apical rotation in genotype positive children with hypertrophic cardiomyopathy
1217   mutations without hypertrophic changes on two-dimensional imaging. J Am Soc
1218   Echocardiogr 27:215-221.
1219   74.   Ho, C. Y., N. K. Sweitzer, B. McDonough, B. J. Maron, S. A. Casey, J. G. Seidman, C. E.
1220   Seidman, and S. D. Solomon. 2002. Assessment of diastolic function with Doppler tissue
1221   imaging to predict genotype in preclinical hypertrophic cardiomyopathy. Circulation
1222   105:2992-2997.
1223   75.   Rüssel, I. K., W. P. Brouwer, T. Germans, P. Knaapen, J. T. Marcus, J. van der Velden, M. J.
1224   Götte, and A. C. van Rossum. 2011. Increased left ventricular torsion in hypertrophic
1225   cardiomyopathy mutation carriers with normal wall thickness. J Cardiovasc Magn Reson
1226   13:3.
1227   76.   Broughton, K. M., J. Li, E. Sarmah, C. M. Warren, Y. H. Lin, M. P. Henze, V. Sanchez-Freire,
1228   R. J. Solaro, and B. Russell. 2016. A myosin activator improves actin assembly and
1229   sarcomere function of human-induced pluripotent stem cell-derived cardiomyocytes with
1230   a troponin T point mutation. American journal of physiology. Heart and circulatory
1231   physiology 311:H107-117.
1232   77.   Nagy, L., A. Kovacs, B. Bodi, E. T. Pasztor, G. A. Fulop, A. Toth, I. Edes, and Z. Papp. 2015.
1233   The novel cardiac myosin activator omecamtiv mecarbil increases the calcium sensitivity
1234   of force production in isolated cardiomyocytes and skeletal muscle fibres of the rat. Br J
1235   Pharmacol.

1236 78. Malik, F. I., J. J. Hartman, K. A. Elias, B. P. Morgan, H. Rodriguez, K. Brejc, R. L. Anderson,
1237   S. H. Sueoka, K. H. Lee, J. T. Finer, R. Sakowicz, R. Baliga, D. R. Cox, M. Garard, G. Godinez,
1238   R. Kawas, E. Kraynack, D. Lenzi, P. P. Lu, A. Muci, C. Niu, X. Qian, D. W. Pierce, M.
1239   Pokrovskii, I. Suehiro, S. Sylvester, T. Tochimoto, C. Valdez, W. Wang, T. Katori, D. A. Kass,
1240   Y. T. Shen, S. F. Vatner, and D. J. Morgans. 2011. Cardiac myosin activation: a potential
1241   therapeutic approach for systolic heart failure. Science 331:1439-1443.
1242 79. Burke, M. A., S. A. Cook, J. G. Seidman, and C. E. Seidman. 2016. Clinical and Mechanistic
1243   Insights Into the Genetics of Cardiomyopathy. Journal of the American College of
1244   Cardiology 68:2871-2886.
1245 80. Moore, J. R., L. Leinwand, and D. M. Warshaw. 2012. Understanding cardiomyopathy
1246   phenotypes based on the functional impact of mutations in the myosin motor. Circulation
1247   research 111:375-385.
1248 81. Davis, J., L. C. Davis, R. N. Correll, C. A. Makarewich, J. A. Schwanekamp, F. Moussavi-
1249   Harami, D. Wang, A. J. York, H. Wu, S. R. Houser, C. E. Seidman, J. G. Seidman, M. Regnier,
1250   J. M. Metzger, J. C. Wu, and J. D. Molkentin. 2016. A Tension-Based Model Distinguishes
1251   Hypertrophic versus Dilated Cardiomyopathy. Cell 165:1147-1159.
1252 82. Bhattacharjee, P., D. Dasgupta, and K. Sengupta. 2017. DCM associated LMNA mutations
1253   cause distortions in lamina structure and assembly. Biochim Biophys Acta Gen Subj
1254   1861:2598-2608.
1255 83. Uhler, C., and G. V. Shivashankar. 2017. Regulation of genome organization and gene
1256   expression by nuclear mechanotransduction. Nat Rev Mol Cell Biol 18:717-727.
1257 84. Iskratsch, T., H. Wolfenson, and M. P. Sheetz. 2014. Appreciating force and shape-the rise
1258   of mechanotransduction in cell biology. Nat Rev Mol Cell Biol 15:825-833.
1259 85. Margossian, S. S., and S. Lowey. 1982. Preparation of myosin and its subfragments from
1260   rabbit skeletal muscle. Methods in enzymology 85 Pt B:55-71.
1261 86. Eads, T. M., D. D. Thomas, and R. H. Austin. 1984. Microsecond rotational motions of
1262   eosin-labeled myosin measured by time-resolved anisotropy of absorption and
1263   phosphorescence. Journal of molecular biology 179:55-81.
1264 87. Spudich, J. A., and S. Watt. 1971. The regulation of rabbit skeletal muscle contraction. I.
1265   Biochemical studies of the interaction of the tropomyosin-troponin complex with actin
1266   and the proteolytic fragments of myosin. The Journal of biological chemistry 246:4866-
1267   4871.
1268 88. Pollard, T. D. 1984. Purification of a high molecular weight actin filament gelation protein
1269   from Acanthamoeba that shares antigenic determinants with vertebrate spectrins. The
1270   Journal of cell biology 99:1970-1980.
1271 89. Greenberg, M. J., T. Lin, Y. E. Goldman, H. Shuman, and E. M. Ostap. 2012. Myosin IC
1272   generates power over a range of loads via a new tension-sensing mechanism. Proceedings
1273   of the National Academy of Sciences of the United States of America 109:E2433-2440.
1274 90. Kozaili, J. M., D. Leek, and L. S. Tobacman. 2010. Dual regulatory functions of the thin
1275   filament revealed by replacement of the troponin I inhibitory peptide with a linker. The
1276   Journal of biological chemistry 285:38034-38041.
1277 91. Hitchcock-DeGregori, S. E., and R. W. Heald. 1987. Altered actin and troponin binding of
1278   amino-terminal variants of chicken striated muscle alpha-tropomyosin expressed in
1279   Escherichia coli. The Journal of biological chemistry 262:9730-9735.

1280   92.   McIntosh, B. B., E. L. Holzbaur, and E. M. Ostap. 2015. Control of the initiation and
1281   termination of kinesin-1-driven transport by myosin-Ic and nonmuscle tropomyosin.
1282   Current biology : CB 25:523-529.
1283   93.   Schindelin, J., I. Arganda-Carreras, E. Frise, V. Kaynig, M. Longair, T. Pietzsch, S. Preibisch,
1284   C. Rueden, S. Saalfeld, B. Schmid, J. Y. Tinevez, D. J. White, V. Hartenstein, K. Eliceiri, P.
1285   Tomancak, and A. Cardona. 2012. Fiji: an open-source platform for biological-image
1286   analysis. Nature methods 9:676-682.
1287   94.   De La Cruz, E. M., and E. M. Ostap. 2009. Kinetic and equilibrium analysis of the myosin
1288   ATPase. Methods in enzymology 455:157-192.
1289   95.   Hsu, P. D., D. A. Scott, J. A. Weinstein, F. A. Ran, S. Konermann, V. Agarwala, Y. Li, E. J.
1290   Fine, X. Wu, O. Shalem, T. J. Cradick, L. A. Marraffini, G. Bao, and F. Zhang. 2013. DNA
1291   targeting specificity of RNA-guided Cas9 nucleases. Nature biotechnology 31:827-832.
1292   96.   Chen, Y. H., and S. M. Pruett-Miller. 2018. Improving single-cell cloning workflow for gene
1293   editing in human pluripotent stem cells. Stem Cell Res 31:186-192.
1294   97.   Sentmanat, M. F., S. T. Peters, C. P. Florian, J. P. Connelly, and S. M. Pruett-Miller. 2018.
1295   A Survey of Validation Strategies for CRISPR-Cas9 Editing. Sci Rep 8:888.
1296   98.   Sharma, A., G. Li, K. Rajarajan, R. Hamaguchi, P. W. Burridge, and S. M. Wu. 2015.
1297   Derivation of highly purified cardiomyocytes from human induced pluripotent stem cells
1298   using small molecule-modulated differentiation and subsequent glucose starvation. J Vis
1299   Exp.
1300   99.   Tse, J. R., and A. J. Engler. 2010. Preparation of hydrogel substrates with tunable
1301   mechanical properties. Curr Protoc Cell Biol Chapter 10:Unit 10 16.
1302